Aerospace Science and Technology

Three-dimensional cooperative integrated guidance and control with fixed-impact time and azimuth constraints

--Manuscript Draft--

Manuscript Number:	AESCTE-D-23-00690
Article Type:	Full length article
Keywords:	Cooperative integrated guidance and control; fixed-impact time constraint; fixed-impact azimuth constraint; 3D reduced-order ESO
Abstract:	A novel three-dimensional (3D) cooperative integrated guidance and control (CIGC) scheme based on backstepping control (BC), sliding mode control (SMC), dynamic surface control (DSC), and a 3D reduced-order extended state observer (ESO) for multiple hypersonic skid-to-turn (STT) missiles simultaneously attacking ground-maneuver targets is proposed in this study, which considers a fixed-impact azimuth and time constraints. First, we established a novel integrated guidance and control (IGC) model that includes the missile-target relative distance and azimuth based on the missile-target engagement dynamics, attitude dynamics, and first-order delay dynamics of the rudder. It is a 3D fifth-order strict-feedback time-varying nonlinear model with mismatched uncertainties. Second, a 3D CIGC scheme was designed, where a cooperative strategy was designed by transforming a fixed-impact time constraint into a nominal range-to-go constraint. The IGC model consists of seeker, guidance, angle-of-attack, attitude, and rudder subsystems based on the BC, and the SMC designs each subsystem. The DSC obtains the derivatives of virtual control commands, which solves the "differential explosion" caused by the BC. The unknown target acceleration, unmodeled parts of the system states, perturbations caused by time-varying parameters, and external disturbances are regarded as lumped disturbances, which are estimated and compensated for by the 3D reduced-order ESO to improve the robustness. Subsequently, the closed-loop system was proven to be stable, and the system states were ultimately uniformly bounded using Lyapunov theory. Finally, the simulation results of three missiles attacking a simultaneously ground-maneuvering target and Monte Carlo simulations demonstrated the effectiveness and robustness of the proposed CIGC scheme.

Three-dimensional cooperative integrated guidance and control with fixed-impact time and azimuth constraints

Zhibing Li [a], Xiaoyue Zhang [a, *], Huanrui Zhang [a], Feng Zhang [b]

[a] *School of Instrumentation and Optoelectronic Engineering, Beihang University, Beijing, 100191, China*

[b] *China North Industries Corp., Beijing, 100029, China*

* Corresponding author: Xiaoyue Zhang

E-mail: zhangxiaoyue@buaa.edu.cn

Tel.: +86-010-8231-6547

Other authors: Zhibing Li, Huanrui Zhang, Feng Zhang.

E-mail address of other authors:

lizhibing@buaa.edu.cn (Zhibing Li);

zhanghr@buaa.edu.cn (Huanrui Zhang);

zhangfeng86@foxmail.com (Feng Zhang).

Abstract

A novel three-dimensional (3D) cooperative integrated guidance and control (CIGC) scheme based on backstepping control (BC), sliding mode control (SMC), dynamic surface control (DSC), and a 3D reduced-order extended state observer (ESO) for multiple hypersonic skid-to-turn (STT) missiles simultaneously attacking ground-maneuver targets is proposed in this study, which considers a fixed-impact azimuth and time constraints. First, we established a novel integrated guidance and control (IGC) model that includes the missile-target relative distance and azimuth based on the missile-target engagement dynamics, attitude dynamics, and first-order delay dynamics of the rudder. It is a 3D fifth-order strict-feedback time-varying nonlinear model with mismatched uncertainties. Second, a 3D CIGC scheme was designed, where a cooperative strategy was designed by transforming a fixed-impact time constraint into a nominal range-to-go constraint. The IGC model consists of seeker, guidance, angle-of-attack, attitude, and rudder subsystems based on the BC, and the SMC designs each subsystem. The DSC obtains the derivatives of virtual control commands, which solves the "differential explosion" caused by the BC. The unknown target acceleration, unmodeled parts of the system states, perturbations caused by time-varying parameters, and external disturbances are regarded as lumped disturbances, which are estimated and compensated for by the 3D reduced-order ESO to improve the robustness. Subsequently, the closed-loop system was proven to be stable, and the system states were ultimately uniformly bounded using Lyapunov theory. Finally, the simulation results of three missiles attacking a simultaneously ground-maneuvering target and Monte Carlo simulations demonstrated the effectiveness and robustness of the proposed CIGC scheme.

Keywords: Cooperative integrated guidance and control; fixed-impact time constraint; fixed-impact azimuth constraint; 3D reduced-order ESO.

1. Introduction

Hypersonic missiles can effectively reduce the detection time of enemy radars and the response time of defense systems, owing to their fast flight speed and high maneuverability. This makes hypersonic missiles an effective weapon to attack key enemy targets. It can also complete various military missions with specific strategic deterrence significance such as surveillance, reconnaissance, and strike operations. Over the past decade, significant progress has been made in hypersonic aerodynamics, thermal protection, and scramjet technologies for hypersonic missiles [1]. The maneuverability and guidance accuracy of the hypersonic missiles improved significantly. However, the survivability and attack effectiveness of single missiles have weakened with recent improvements in the missile defense systems. Salvo attacks on multiple missiles have become an effective method to improve the possibility of penetration. The simultaneous attack of multiple missiles against a target can effectively increase the survivability of the missiles and the probability of destruction against the target, thus becoming the subject of this research topic.

The current research on multimissile salvo guidance and control algorithms can be divided into two categories. The first category is a simultaneous attack on the time scale, that is, the individual homing guidance mode that satisfies the fixed-impact time constraint. The advantage of this guidance strategy is that there is no dynamic information interaction between missiles during engagement, nor is there a communication topology required between the missiles. This constitutes the open-loop guidance strategy. Because no communication link between missiles is required during missile-target engagement, multiple missiles can achieve simultaneous attacks when encountering electronic interference from the enemy. This guidance strategy is commonly used in guidance law designs with a fixed-impact-time constraint. A fixed-impact time-constrained guidance law (ITCG) was first applied in [2], where an ITCG was proposed for stationary targets based on the proportional guidance law (PNG) and desired impact-time error. Subsequently, many scholars have conducted studies on

ITCG. In [3], an ITCG was proposed using a time-varying PNG and bias feedback command. The proposed time-to-go estimation based on time-varying PNG is more accurate than the time-to-go estimation calculated using conventional PNG. In [4], a three-stage PNG was proposed in [4], which achieved the impact-time constraint by designing different guidance constants to change the ballistic trajectory. Based on the impact-time constraint, many scholars have proposed guidance laws that satisfy other constraints such as the angle-of-attack [5] and field-of-view (FOV) constraints [6]. Based on an optimal control algorithm, [7] proposed an impact-angle-constrained guidance law and matched time-to-go estimation algorithm. It implements an impact-time constraint by adding a feedback control term. In [8], a two-stage guidance law was proposed to achieve impact time and angle constraints, where a switching strategy ensured the connection of the two-stage guidance law. Reference [9] proposed a guidance law that satisfied both the impact time and FOV constraints based on a time-varying sliding mode control (SMC), where the time-to-go estimation avoided the small-angle assumption. With PNG and biased PNG, [10] proposed a three-dimensional (3D) impact-time guidance law and simultaneously satisfied the FOV constraint, where the bias term ensured that the missile intercepted the target within the desired attack time. In literature [11], a 3D time-to-go estimation was proposed and the FOV constraint was achieved by adding a bias term to a 3D PNG.

The aforementioned studies were mainly conducted for stationary or slow-moving targets, and all relied on time-to-go estimation. However, it is difficult to accurately estimate time-to-go, particularly for maneuvering targets. If the time-to-go estimation has a large error, guidance strategies may fail and even lead to missing a target. Some studies have attempted to design guidance laws with impact-time constraints without using a time-to-go prediction formula. Reference [12] proposed a cruise guidance law that satisfied both the impact angle and time constraints and achieved the impact-time constraint by controlling the missile trajectory, thus avoiding the use of time-to-go prediction. Reference [13] proposed a guidance law based on two different nonsingular

terminal sliding mode controls that satisfy the impact angle and time constraints. The time-to-go estimation was revised using the predicted intercept point to achieve interception of constant acceleration targets. Reference [14] achieved the desired impact time by tracking a time-varying line-of-sight (LOS) profile, which enabled a strike against a maneuvering target owing to the accurate estimation of the unknown acceleration of the target using the inertial-delay control method. In [15] a 3D guidance law was designed with an impact-time constraint for moving targets.

The second category is cooperative homing guidance, which achieves distance or position agreement with real-time communication topology between missiles. Specifically, in missile-target engagement, real-time data are transmitted between missiles through a communication topology. Each missile generates cooperative commands to achieve a simultaneous attack based on the position information of the adjacent missiles. The consensus of multiagent systems is often used to design cooperative guidance laws to achieve time-to-go or position agreement. Reference [16] proposed a 3D adaptive fixed-time cooperative guidance law with an impact angle constraint, where the fixed-time consensus theory was used to ensure agreement of the time-to-go estimation errors of missiles. Graph theory proved that communication topology switching failures did not affect the proposed guidance law. A cooperative guidance law considering the impact angle constraint was proposed in [17], in which a finite-time consensus protocol was used to design acceleration commands along the LOS to ensure that all missiles simultaneously attacked the maneuvering target. In the second stage, the acceleration commands in the direction normal to the LOS were designed based on the adaptive fast-terminal SMC to ensure the achievement of the impact angle constraint. A cooperative guidance law considering the FOV constraint was proposed by centralized and distributed communication topologies in the literature [18], where a centralized leader-follower structure was used for communication within the group and a distributed communication topology was used for communication between the leaders of each group. In [19], a 3D cooperative guidance law based on a

distributed communication topology was proposed using the multiagent systems consensus theory to guarantee time-to-go agreement. In literature [20], a 3D cooperative guidance law with an impact angle constraint was proposed based on a distributed communication topology. The distributed sliding mode surface required only state information from adjacent missiles, and the multiagent system consensus theory ensured the agreement of range-to-go for all missiles and avoided the estimation error of time-to-go. Reference [21] proposed a leader-follower cooperative guidance strategy in which only the leader missile is equipped with a seeker. The leader adopts a guidance law that satisfies the prespecified impact time, and the follower adopts a cooperative guidance law that ensures proportional consensus with the leader's range-to-go.

The aforementioned guidance strategies are primarily based on the relative motion of the missile-target, and derive normal overloads to achieve the impact-time constraint. The above guidance laws are designed under the assumption of spectral separation, that is, assuming that the dynamics of missiles are ideal or that the time constant of the control loop (autopilot) is much smaller than that of the guidance loop; thus, the control loop can be ignored in the design. However, the missile-target distance changes rapidly during the terminal guidance phase, and the dynamics of the missile control loop significantly affect the response time of the guidance loop. The traditional design method of separating guidance and control loops (SGC) may lead to performance degradation of the guidance control system, which may become unstable [22]. The integrated guidance and control (IGC) design method treats the guidance and control loops as a whole and derives control commands directly based on the missile-target motion relation and missile dynamics. It has been shown that the IGC method can fully exploit the coupling effect between the guidance and control loops compared to the SGC method, which is conducive to improving the stability of the entire guidance control system and reducing the miss distance [23]. Additionally, the IGC method can shorten the design cycle and improve economy and reliability [24]. For the

cooperative integrated guidance and control (CIGC) design scheme with simultaneous attacks, some scholars have attempted to establish the dynamic characteristics of the time-to-go by missile time-to-go formulation and dynamics, establish the sliding mode surface with time-to-go estimation errors, and derive rudder control commands [25-26]. In [27], a missile time-to-go dynamic formulation was established. The leader-follower and no-leader modes were designed to determine whether the impact time was predefined or set in the engagement. The other category achieves a simultaneous attack by establishing a higher-order IGC model and then designing it using backstepping control (BC) and SMC. In [28], an IGC model with a target look angle was established. Subsequently, a simultaneous attack with a predefined impact time was achieved by tracking the error between the actual and nominal range-to-go. In [29], a 3D IGC model containing the heading error was established, and a partial integrated guidance and control approach was proposed, in which a simultaneous attack was achieved by tracking the average distance of all missiles. In [30], the desired lateral accelerations were derived using the bias-tracking guidance law. The virtual commands of the guidance loop are then accurately tracked by an autopilot to achieve a simultaneous attack with a predefined impact time. In [31], an IGC design scheme with an impact angle constraint was proposed, and a formulation was designed to estimate the impact time. This allows adjustment of the missile controller parameters to achieve a predefined impact time.

In summary, simultaneous attacks with a fixed-impact time were primarily considered in the guidance law design. However, the guidance law is usually designed with the assumption of ideal autopilot dynamic characteristics, which is equivalent to ignoring the autopilot dynamics. The characteristics of the terminal guidance phase of hypersonic missiles are fast time varying and strong disturbances, and the dynamic characteristics of the autopilot significantly affect the response speed of the missiles, which must be considered. The CIGC can fully consider the coupling effect between the guidance and control loops, thereby effectively improving the performance of the

guidance control system. Most CIGC schemes with fixed-impact times have been designed based on missile time-to-go estimation. However, it is difficult to accurately estimate the time-to-go for maneuvering the targets. Therefore, when there was a large deviation between the estimated and actual time-to-go, the terminal-impact time also exhibited a large deviation. Moreover, most of the aforementioned CIGC schemes consider only the saturation input constraint and regard the controller output as the actual rudder angle; that is, the dynamic characteristics of the rudders are ideal and the delay dynamics of the rudders are neglected. As the only actuator in the terminal guidance phase of hypersonic missiles, the rudder delay dynamics also affect the response speed of the missile guidance control system and therefore needs to be considered in the design. Additionally, if multiple missiles can approach and attack the target at different azimuths, the probability of penetration is significantly enhanced, and the damaging effect is amplified. For all intents and purposes, the CIGC of hypersonic missiles attacking ground-maneuvering targets and considering the constraints of rudder delay dynamics and saturation, fixed-impact azimuth, and fixed-impact time has never been observed in previous studies.

Inspired by the above analysis, based on SMC, BC, dynamic surface control (DSC), and 3D reduced-order extended state observer (ESO), this study proposes a novel 3D CIGC scheme with fixed-impact azimuth and fixed-impact time constraints for multiple hypersonic skid-to-turn (STT) missiles attacking a ground-maneuvering target. Moreover, to ensure robustness, the perturbations caused by variations in the aerodynamic parameters, unmodeled parts of the system states, external disturbances, and target maneuvers were regarded as lumped disturbances that were estimated using a 3D reduced-order ESO. Compared to the existing results on CIGC schemes, the main contributions of this study can be summarized as follows.

1) In contrast to the literature [13, 25, 27, 30], the proposed 3D CIGC scheme simultaneously considers the fixed-impact time, rudder delay dynamics and saturation, and impact azimuth constraints, which have not been simultaneously

satisfied in previous studies.

2) In this study, a novel cooperative strategy was designed by transforming a fixed-impact time constraint into a nominal range-to-go constraint. Subsequently, a novel 3D strict-feedback nonlinear IGC model with mismatched uncertainties was established, containing the missile-target distance, missile-target azimuth, attitude dynamics equations of missiles, and a first-order delay model of the rudder.

3) A 3D CIGC controller was designed based on SMC, BC, and DSC. First, based on the BC, the guidance control system consists of seeker, guidance, angle-of-attack, attitude, and rudder subsystems. The lumped disturbances in the system model are estimated and compensated for by the 3D reduced-order ESO to ensure the robustness of the proposed CIGC scheme, which also avoids switching terms in the controller, thus avoiding the "chattering" caused by the SMC.

4) Lyapunov theory proves the stability of the closed-loop system and uniformly bounded system states. The numerical simulation results also proved the effectiveness and robustness of the proposed scheme.

The remainder of this paper is organized as follows. Section 2 presents the 3D IGC model derivation process and control objective design. Section 3 elaborates on the cooperative strategy and the 3D CIGC scheme. The stability of the closed-loop system is described in Section 4. Section 5 presents the simulation results and data analysis. Finally, the conclusions of this study are summarized in Section 6.

2. Model design and control objectives

Aiming at hypersonic missiles attacking ground-maneuvering targets, a 3D nonlinear strict-feedback IGC model was established based on missile-target engagement kinematics, dynamic equations, and rudder first-order delay models. The design objectives of this study were as follows.

2.1 Problem formulation

The missile-target engagement geometry in a 3D space coordinate system is shown in Fig. 1. M and T denote the missile and the target, respectively. $Ox_1y_1z_1$ is an Earth-fixed inertial coordinate system. $Mx_4y_4z_4$ is the missile LOS coordinate system attached to the missile, where Mx_4 is coincident with the LOS, and the positive direction points toward the target. My_4 lies in the longitudinal plane containing the Mx_4 axis, is perpendicular to the Mx_4 axis, upwards is defined as positive. The Mz_4 axis is perpendicular to the Mx_4y_4 plane, and follows the right-hand rule. The elevation and azimuth angles of the LOS are denoted as q_1 and q_2, respectively, and are defined counterclockwise as positive. The missile flight path and azimuth angles are denoted by θ_M and ψ_{VM}, respectively, and their counterclockwise directions are positive.

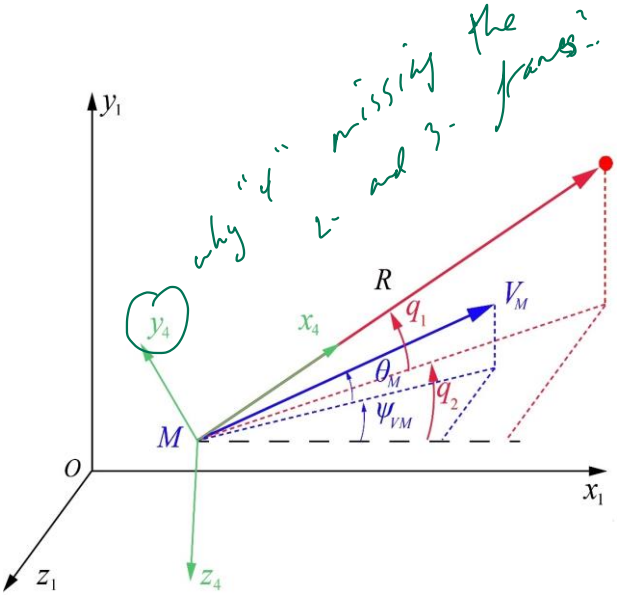

Fig. 1. Three-dimensional missile-target engagement geometry

Assumption. 1. For an easy modeling analysis, the missile can be simplified to a perfect point motion during engagement in the terminal guidance phase.

Assumption. 2. In the terminal guidance phase, the missile thrust is zero and the velocity of the missile is constant. In other words, the variation in the missile velocity can be regarded as an unmodeled part of the system states.

The relative distance, velocity, and acceleration vectors between the missile and target are denoted as $\mathbf{R}$, $\mathbf{V}_R$, and $\mathbf{a}_R$, respectively. According to the Coriolis theorem, the following equations can be derived as follows:

$$\mathbf{V}_\mathbf{R} = \frac{\partial \mathbf{R}}{\partial t} + \mathbf{\Omega} \times \mathbf{R}, \tag{1}$$

$$\mathbf{a}_\mathbf{R} = \frac{\partial \mathbf{V}_\mathbf{R}}{\partial t} + \mathbf{\Omega} \times \mathbf{V}_\mathbf{R}, \tag{2}$$

where $\mathbf{V}_R = [V_{Rx4}\ V_{Ry4}\ V_{Rz4}]^T$, $\mathbf{R} = [R\ 0\ 0]^T$, $\mathbf{a}_R = [a_{Rx4}\ a_{Ry4}\ a_{Rz4}]^T$. $\mathbf{\Omega} = [\dot{q}_2 \sin q_1\ \dot{q}_2 \cos q_1\ \dot{q}_1]^T$ is the angular velocity vector of the LOS coordinate system with respect to the inertial coordinate system.

Equation (1) can be derived as

$$\mathbf{V}_\mathbf{R} = \begin{bmatrix} V_{Rx4} \\ V_{Ry4} \\ V_{Rz4} \end{bmatrix} = \begin{bmatrix} \dot{R} \\ 0 \\ 0 \end{bmatrix} + \begin{bmatrix} 0 & \dot{q}_1 & \dot{q}_2 \cos q_1 \\ \dot{q}_1 & 0 & -\dot{q}_2 \sin q_1 \\ -\dot{q}_2 \cos q_1 & \dot{q}_2 \sin q_1 & 0 \end{bmatrix} \begin{bmatrix} R \\ 0 \\ 0 \end{bmatrix} = \begin{bmatrix} \dot{R} \\ R\dot{q}_1 \\ -R\dot{q}_2 \cos q_1 \end{bmatrix}. \tag{3}$$

Substituting Eq. (3) into Eq. (2) yields

$$\mathbf{a}_R = \mathbf{a}_{T4} - \mathbf{a}_{M4} = \begin{bmatrix} a_{Tx4} \\ a_{Ty4} \\ a_{Tz4} \end{bmatrix} - \begin{bmatrix} a_{Mx4} \\ a_{My4} \\ a_{Mz4} \end{bmatrix} = \begin{bmatrix} \ddot{R} - R\dot{q}_1^2 - R\dot{q}_2^2 \cos^2 q_1 \\ 2\dot{R}\dot{q}_1 + R\ddot{q}_1 + R\dot{q}_2^2 \sin q_1 \cos q_1 \\ -R\ddot{q}_2 \cos q_1 - 2\dot{R}\dot{q}_2 \cos q_1 + 2R\dot{q}_1\dot{q}_2 \sin q_1 \end{bmatrix}, \tag{4}$$

where $\mathbf{a}_{T4} = \left[a_{Tx4}, a_{Ty4}, a_{Tz4}\right]^T$ and $\mathbf{a}_{M4} = \left[a_{Mx4}, a_{My4}, a_{Mz4}\right]^T$ denote the acceleration vectors of the target and missile in the LOS coordinate system, respectively.

According to the Coriolis theorem, the missile acceleration vector in the LOS coordinate system can be expressed as

$$\mathbf{a}_{M4} = \frac{\partial \mathbf{V}_{M4}}{\partial t} + \mathbf{\Omega} \times \mathbf{V}_{M4}, \tag{5}$$

where $\mathbf{V}_{M4}=[V_{Mx4}\ V_{My4}\ V_{Mz4}]^T$ is the velocity vector of the missile in the LOS coordinate system.

The velocity vector of the missile $\mathbf{V}_M$ in the inertial coordinate system is expressed as follows:

$$\mathbf{V}_M=\begin{bmatrix}V_{Mx}\\V_{My}\\V_{Mz}\end{bmatrix}=\begin{bmatrix}V_M\cos\theta_M\cos\psi_{VM}\\V_M\sin\theta_M\\-V_M\cos\theta\sin\psi_{VM}\end{bmatrix}. \tag{6}$$

According to the geometry between the inertial coordinate system and the LOS coordinate system, the coordinate transformation matrix can be obtained as

$$L(q_2,q_1)=\begin{bmatrix}\cos q_1\cos q_2 & \sin q_1 & -\cos q_1\sin q_2\\-\sin q_1\cos q_2 & \cos q_1 & \sin q_1\sin q_2\\\sin q_2 & 0 & \cos q_2\end{bmatrix}. \tag{7}$$

Therefore, the velocity vector of the missile in the LOS coordinate system can be derived as

$$\mathbf{V}_{M4}=L(q_2,q_1)\mathbf{V}_M=\begin{bmatrix}V_{Mx4}\\V_{My4}\\V_{Mz4}\end{bmatrix}=\begin{bmatrix}V_M\cos\theta_M\cos q_1\cos(q_2-\psi_{VM})+V\sin\theta_M\sin q_1\\-V_M\cos\theta_M\sin q_1\cos(q_2-\psi_{VM})+V\sin\theta_M\cos q_1\\V_M\cos\theta_M\sin(q_2-\psi_{VM})\end{bmatrix}. \tag{8}$$

Substituting Eq. (8) into Eq. (5) yields

$$\mathbf{a}_{M4}=\begin{bmatrix}a_{Mx4}\\a_{My4}\\a_{Mz4}\end{bmatrix}=\begin{bmatrix}V_M\dot\theta_M\left[\cos\theta_M\sin q_1-\sin\theta_M\cos q_1\cos(q_2-\psi_{VM})\right]\\+V_M\cos\theta_M\dot\psi_{VM}\cos q_1\sin(q_2-\psi_{VM})\\V_M\dot\theta_M\left[\cos\theta_M\cos q_1+\sin\theta_M\sin q_1\cos(q_2-\psi_{VM})\right]\\-V_M\cos\theta_M\dot\psi_{VM}\sin q_1\sin(q_2-\psi_{VM})\\-V_M\dot\theta_M\sin\theta_M\sin(q_2-\psi_{VM})-V_M\cos\theta_M\dot\psi_{VM}\cos(q_2-\psi_{VM})\end{bmatrix}. \tag{9}$$

Substituting Eq. (9) into Eq. (4) yields

$$\begin{aligned}\ddot R=R\dot q_1^2+R\dot q_2^2\cos^2 q_1-V_M\dot\theta_M\left[\cos\theta_M\sin q_1-\sin\theta_M\cos q_1\cos(q_2-\psi_{VM})\right]\\-V_M\cos\theta_M\dot\psi_{VM}\cos q_1\sin(q_2-\psi_{VM})+a_{Tx4}\end{aligned}, \tag{10}$$

$$\begin{aligned}\ddot q_1=-\frac{2\dot R\dot q_1}{R}-\dot q_2^2\sin q_1\cos q_1-\frac{V_M\dot\theta_M}{R}\left[\cos\theta_M\cos q_1+\sin\theta_M\sin q_1\cos(q_2-\psi_{VM})\right]\\+\frac{V_M\cos\theta_M\dot\psi_{VM}}{R}\sin q_1\sin(q_2-\psi_{VM})+\frac{a_{Ty4}}{R}\end{aligned}, \tag{11}$$

$$\ddot{q}_2 = -\frac{2\dot{R}\dot{q}_2}{R} + 2\dot{q}_1\dot{q}_2\tan q_1 - \frac{V_M\dot{\theta}_M}{R\cos q_1}\sin\theta_M\sin\left(q_2-\psi_{VM}\right) - \frac{V_M\cos\theta_M\dot{\psi}_{VM}}{R\cos q_1}\cos\left(q_2-\psi_{VM}\right) - \frac{a_{Tz4}}{R\cos q_1} \quad (12)$$

The dynamics equation of the missile can be expressed as

$$\begin{cases}\dot{\theta}_M = \dfrac{Y\cos\gamma_V - Z\sin\gamma_V - mg\cos\theta_M}{mV_M} \\ \dot{\psi}_{VM} = \dfrac{-Y\sin\gamma_V - Z\cos\gamma_V}{mV_M\cos\theta_M}\end{cases} \quad (13)$$

Assumption. 3. For STT missiles, one control objective is to maintain γ_V stabilized near zero to ensure flight stability. That is, γ_V can be reasonably approximated as $\sin\gamma_V \approx 0$, $\cos\gamma_V \approx 1$.

Define $f_{R1} = \cos\theta_M\sin q_1 - \sin\theta_M\cos q_1\cos\left(q_2-\psi_{VM}\right)$, $f_{R2} = \cos q_1\sin\left(q_2-\psi_{VM}\right)$, $f_{\varepsilon 1} = \left[\cos\theta_M\cos q_1 + \sin\theta_M\sin q_1\cos\left(q_2-\psi_{VM}\right)\right]/R$, $f_{\varepsilon 2} = \sin q_1\sin\left(q_2-\psi_{VM}\right)/R$, $f_{\eta 1} = \dfrac{\sin\theta_M\sin\left(q_2-\psi_{VM}\right)}{R\cos q_1}$, $f_{\eta 2} = \dfrac{\cos\left(q_2-\psi_{VM}\right)}{R\cos q_1}$. According to Assumption 3, by substituting Eq. (13) into Eqs. (10)–(12) yields

$$\ddot{R} = R\dot{q}_1^2 + R\dot{q}_2^2\cos^2 q_1 - f_{R1}\frac{Y-mg\cos\theta_M}{m} + f_{R2}\frac{Z}{m} + a_{Tx4}, \quad (14)$$

$$\ddot{q}_1 = -\frac{2\dot{R}\dot{q}_1}{R} - \dot{q}_2^2\sin q_1\cos q_1 - f_{\varepsilon 1}\frac{Y-mg\cos\theta_M}{m} - f_{\varepsilon 2}\frac{Z}{m} + \frac{a_{Ty4}}{R}, \quad (15)$$

$$\ddot{q}_2 = -\frac{2\dot{R}\dot{q}_2}{R} + 2\dot{q}_1\dot{q}_2\tan q_1 - f_{\eta 1}\frac{Y-mg\cos\theta_M}{m} + f_{\eta 2}\frac{Z}{m} - \frac{a_{Tz4}}{R\cos q_1}. \quad (16)$$

The aerodynamic forces and aerodynamic moments of missiles can be approximated as

$$\begin{cases} Y = c_y^{\alpha}QS\alpha + d_Y \\ Z = c_z^{\beta}QS\beta + d_Z \end{cases}, \quad (17)$$

$$\begin{cases} M_x = \left(m_x^{\alpha}\alpha + m_x^{\beta}\beta + m_x^{\delta_x}\delta_X\right)QSL + d_{M_x} \\ M_y = \left(m_y^{\beta}\beta + m_y^{\delta_y}\delta_y\right)QSL + d_{M_y} \\ M_z = \left(m_z^{\alpha}\alpha + m_z^{\delta_z}\delta_z\right)QSL + d_{M_z} \end{cases}, \tag{18}$$

where d_Y, d_Z, d_{M_x}, d_{M_y}, and d_{M_z} are the aerodynamic parameter errors due to the approximation. $Q = \frac{1}{2}\rho V_m^2$ is the dynamic pressure and ρ is the atmospheric density.

Substituting Eq. (17) into Eqs. (14)–(16) yields

$$\ddot{R} = R\dot{q}_1^2 + R\dot{q}_2^2\cos^2 q_1 + f_{R1}g\cos\theta_M - f_{R1}\frac{c_Y^{\alpha}QS\alpha}{m} + f_{R2}\frac{c_Z^{\beta}QS\beta}{m} + \Delta_R, \tag{19}$$

$$\ddot{q}_1 = -\frac{2\dot{R}\dot{q}_1}{R} - \dot{q}_2^2\sin q_1\cos q_1 + f_{\varepsilon 1}g\cos\theta_M - f_{\varepsilon 1}\frac{c_Y^{\alpha}QS\alpha}{m} - f_{\varepsilon 2}\frac{c_Z^{\beta}QS\beta}{m} + \Delta_{q_1}, \tag{20}$$

$$\ddot{q}_2 = -\frac{2\dot{R}\dot{q}_2}{R} + 2\dot{q}_1\dot{q}_2\tan q_1 + f_{\eta 1}g\cos\theta_M - f_{\eta 1}\frac{c_Y^{\alpha}QS\alpha}{m} + f_{\eta 2}\frac{c_Z^{\beta}QS\beta}{m} + \Delta_{q_2}. \tag{21}$$

The attitude dynamics equation of the missile can be given as

$$\begin{cases} \dot{\alpha} = -\omega_x\tan\beta\cos\alpha + \omega_y\tan\beta\sin\alpha + \omega_z \\ \qquad -\dfrac{Y}{mV_M\cos\beta} + \dfrac{g\cos\theta_M\cos\gamma_V}{V_M\cos\beta} + d_\alpha \\ \dot{\beta} = \omega_x\sin\alpha + \omega_y\cos\alpha + \dfrac{Z}{mV_M} + \dfrac{g\cos\theta_M\sin\gamma_V}{V_M} + d_\beta \\ \dot{\gamma}_V = \omega_x\cos\alpha\sec\beta - \omega_y\sin\alpha\sec\beta - \dfrac{g\cos\theta_M\cos\gamma_V\tan\beta}{V_M} \\ \qquad + \dfrac{Y\left(\tan\theta_M\sin\gamma_v + \tan\beta\right) + Z\tan\theta_M\cos\gamma_v}{mV_M} + d_{\gamma_V} \end{cases}, \tag{22}$$

$$\begin{cases} \dot{\omega}_x = \dfrac{J_y - J_z}{J_x}\omega_z\omega_y + \dfrac{M_x}{J_x} + d_{\omega_x} \\ \dot{\omega}_y = \dfrac{J_z - J_x}{J_y}\omega_x\omega_z + \dfrac{M_y}{J_y} + d_{\omega_y} \\ \dot{\omega}_z = \dfrac{J_x - J_y}{J_z}\omega_y\omega_x + \dfrac{M_z}{J_z} + d_{\omega_z} \end{cases}. \tag{23}$$

If the missile rudder is simplified to a first-order system, the rudder model can be expressed as follows

$$\begin{aligned}\delta_{xc} &= \tau_x\dot{\delta}_x + \delta_x \\ \delta_{yc} &= \tau_y\dot{\delta}_y + \delta_y \\ \delta_{zc} &= \tau_z\dot{\delta}_z + \delta_z\end{aligned} \tag{24}$$

Owing to the physical limitations of the rudder, the controller commands should satisfy the following saturation function to ensure that the rudder amplitudes do not exceed the maximum limit.

$$sat(\delta_{ic}) = \begin{cases}\delta_i^{\max} sign(\delta_{ic}), & |\delta_{ic}| > \delta_i^{\max} \\ \delta_{ic}, & |\delta_{ic}| \le \delta_i^{\max}\end{cases} \quad i = x, y, z \tag{25}$$

Based on the assumptions above and model approximations, Eqs. (19)–(25), the 3D nonlinear strict-feedback IGC model with mismatched uncertainties can be summarized as follows:

$$\begin{cases}\dot{\mathbf{x}}_0 = \mathbf{x}_1 \\ \dot{\mathbf{x}}_1 = \mathbf{F}_1 + \mathbf{G}_1\mathbf{x}_2^* + \mathbf{d}_1 \\ \dot{\mathbf{x}}_2 = \mathbf{F}_2 + \mathbf{G}_2\mathbf{x}_3 + \mathbf{d}_2 \\ \dot{\mathbf{x}}_3 = \mathbf{F}_3 + \mathbf{G}_3\mathbf{x}_4 + \mathbf{d}_3 \\ \dot{\mathbf{x}}_4 = \mathbf{F}_4 + \mathbf{G}_4\,\mathrm{sat}(\mathbf{u})\end{cases} \tag{26}$$

where the system state vectors are $\mathbf{x}_0 = [R, q_2]^T$, $\mathbf{x}_1 = [\dot{R}, \dot{q}_2]^T$, $\mathbf{x}_2^* = [\alpha, \beta]^T$, $\mathbf{x}_2 = [\alpha, \beta, \gamma_V]^T$, $\mathbf{x}_3 = [\omega_x, \omega_y, \omega_z]^T$ and $\mathbf{x}_4 = [\delta_x, \delta_y, \delta_z]^T$. The control input vector is $\mathbf{u} = [\delta_{xc}, \delta_{yc}, \delta_{zc}]^T$. $\mathbf{d}_1$, $\mathbf{d}_2$, and $\mathbf{d}_3$ are lumped disturbances. The remaining nonlinear functions are expressed as

$$\mathbf{F}_1 = \begin{bmatrix} R\dot{q}_1^2 + R\dot{q}_2^2\cos^2 q_1 + f_{R1}g\cos\theta_M \\ -\dfrac{2\dot{R}\dot{q}_2}{R} + 2\dot{q}_1\dot{q}_2\tan q_1 + f_{\eta 1}g\cos\theta_M \end{bmatrix}^T,$$

$$\mathbf{G}_1 = \begin{bmatrix} -f_{R1}\dfrac{c_y^\alpha QS}{m} & f_{R2}\dfrac{c_z^\beta QS}{m} \\ -f_{\eta 1}\dfrac{c_y^\alpha QS}{m} & f_{\eta 2}\dfrac{c_z^\beta QS}{m} \end{bmatrix}^T,$$

315 $$\mathbf{F}_2=\begin{bmatrix} -\dfrac{Y}{mV_M\cos\beta}+\dfrac{g\cos\theta_M\cos\gamma_V}{V_M\cos\beta} \\ \dfrac{Z}{mV_M}+\dfrac{g\cos\theta_M\sin\gamma_V}{V_M} \\ -\dfrac{g\cos\theta_M\cos\gamma_V\tan\beta}{V_M}+\dfrac{Z\tan\theta_M\cos\gamma_V+Y\left(\tan\theta_M\sin\gamma_v+\tan\beta\right)}{mV_M} \end{bmatrix}^T,$$

316 $$\mathbf{G}_2=\begin{bmatrix} -\tan\beta\cos\alpha & \tan\beta\sin\alpha & 1 \\ \sin\alpha & \cos\alpha & 0 \\ \cos\alpha\sec\beta & -\sin\alpha\sec\beta & 0 \end{bmatrix}^T,$$

317 $$\mathbf{F}_3=\begin{bmatrix} \dfrac{J_y-J_z}{J_x}\omega_z\omega_y+\dfrac{QSL\left(m_x^{\alpha}\alpha+m_x^{\beta}\beta\right)}{J_x} \\ \dfrac{\left(J_z-J_x\right)\omega_x\omega_z}{J_y}+\dfrac{QSLm_y^{\beta}\beta}{J_y} \\ \dfrac{\left(J_x-J_y\right)\omega_y\omega_x}{J_z}+\dfrac{QSLm_z^{\alpha}\alpha}{J_z} \end{bmatrix}^T,$$

318 $$\mathbf{G}_3=\begin{bmatrix} \dfrac{m_x^{\delta_x}}{J_x} & 0 & 0 \\ 0 & \dfrac{m_y^{\delta_y}}{J_y} & 0 \\ 0 & 0 & \dfrac{m_z^{\delta_z}}{J_z} \end{bmatrix}^T,$$

319 $$\mathbf{F}_4=\begin{bmatrix} -\dfrac{1}{\tau_x}\delta_x \\ -\dfrac{1}{\tau_y}\delta_y \\ -\dfrac{1}{\tau_z}\delta_z \end{bmatrix}^T,$$

320 $$\mathbf{G}_4=\begin{bmatrix} \dfrac{1}{\tau_x} & 0 & 0 \\ 0 & \dfrac{1}{\tau_y} & 0 \\ 0 & 0 & \dfrac{1}{\tau_z} \end{bmatrix}^T.$$

321 The errors between the saturation function and actual control command can be

322 expressed as $\text{sat}(\mathbf{u}) = \mathbf{u} + \triangle\mathbf{u}$. Substituting this into the fifth equation of Eq. (26) yields

$$\begin{aligned}\dot{\mathbf{x}}_4 &= \mathbf{F}_4 + \mathbf{G}_4 \,\text{sat}(\mathbf{u}) \\ &= \mathbf{F}_4 + \mathbf{G}_4(\mathbf{u} + \triangle\mathbf{u}) \\ &= \mathbf{F}_4 + \mathbf{G}_4\mathbf{u} + \mathbf{d}_4\end{aligned} \tag{27}$$

324 **Remark. 1.** $\mathbf{d}_1$ is primarily affected by the time-varying perturbation errors of the
325 aerodynamic parameters and target maneuvers. $\mathbf{d}_2$ and $\mathbf{d}_3$ mainly contain the time-
326 varying perturbation errors of the aerodynamic parameters and unmodeled parts of the
327 system states. $\mathbf{d}_4$ mainly contains errors caused by the saturation function and rudder
328 actuation.

329 **Remark. 2.** Owing to the continuous and bounded aerodynamic parameters of the
330 missile as well as the maneuverability of the target, the lumped disturbances of the
331 system are also continuous and bounded.

332 **Assumption. 4.** The system-lumped disturbances $\mathbf{d}_i, i = 1,2,3,4$ and their derivatives
333 are continuous and bounded; however, their upper boundaries are unknown.

334 **Assumption. 5.** There is $\dot{R}(t)<0$ in the terminal guidance phase. Moreover, since the
335 missile and target have a non-zero size, there exist positive numbers $R_{\min}$ and $R_{\max}$
336 satisfying $R_{\min} < R(t_f) < R_{\max}$ at the interception point, and $R(t_f)$ is the distance
337 between the missile and the target at the interception point.

338 **2.2 Design objectives**

339 For hypersonic STT missiles, in addition to satisfying the saturation constraint and
340 rudder delay dynamics, the IGC controller for the strict-feedback IGC model proposed
341 in Eqs. (26) and (27) should satisfy the following design objectives:

342 a) The miss distance should be less than 1 m.
343 b) The error between the impact time of each missile and predefined impact time
344 should be less than 0.1 s.
345 c) The error between the terminal azimuth of each missile and the predefined

azimuth was less than 0.5°.

d) The designed CIGC scheme must be robust in the presence of unknown lumped disturbances.

3. Design of three-dimensional cooperative integrated guidance and control

In this section, a 3D CIGC scheme that considers the fixed-impact azimuth and fixed-impact time constraints is proposed. The 3D IGC model Eqs. (26) and (27) are time-varying nonlinear fifth-order strict-feedback systems with mismatched uncertainties. The BC consists of seeker, guidance, angle-of-attack, attitude, and rudder subsystems. Subsequently, each subsystem was designed using the SMC. The "differential explosion" phenomenon caused by the BC is solved by introducing the DSC. To ensure robustness, the lumped disturbances in the system were estimated using a 3D reduced-order ESO and compensated for in the control law. The designed CIGC control scheme is shown in Fig. 2.

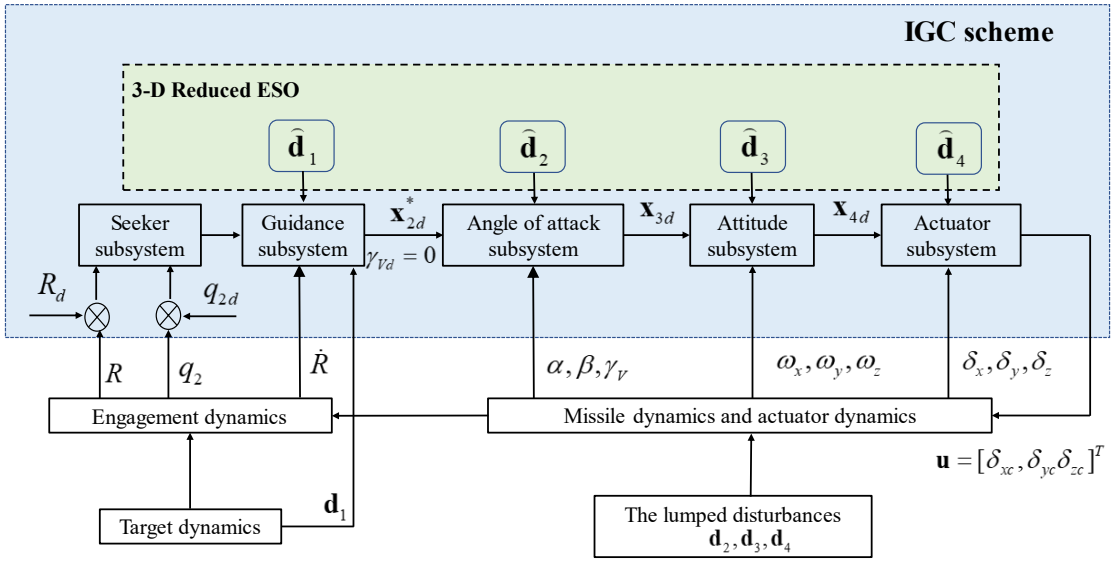

Fig. 2. Schematic diagram of the 3-D CIGC

The following vector calculations were performed to facilitate the derivation of the formula: For vectors $\mathbf{a}=[a_1,a_2,\cdots,a_n]^T$ and $\mathbf{b}=[b_1,b_2,\cdots,b_n]^T$, we have

$\dot{\mathbf{a}}=[\dot{a}_1,\dot{a}_2,\cdots,\dot{a}_n]^T$,

$\mathbf{a}^{\mathbf{b}}=[a_1^{b_1},a_2^{b_2},\cdots,a_n^{b_n}]^T$,

$\mathbf{a}./\mathbf{b}=[a_1/b_1,a_2/b_2,\cdots,a_n/b_n]^T$,

$\mathrm{sgn}^{\delta}(\mathbf{a})=[|a_1|^{\delta}\,\mathrm{sign}(a_1),|a_2|^{\delta}\,\mathrm{sign}(a_2),\cdots,|a_n|^{\delta}\,\mathrm{sign}(a_n)]^T$,

$\mathrm{diag}(\mathbf{a}./\mathbf{b})=\mathrm{diag}(a_1/b_1,a_2/b_2,\cdots,a_n/b_n)$.

3.1 Design of cooperative strategy

Simultaneous attacks based on a predefined time require multiple missiles to simultaneously hit a target. The design process is explained below, using a missile as an example. Assuming that the desired impact time is T_d, the nominal range-to-go can be defined as:

$$R_d = \gamma V_m (T_d - t), \tag{28}$$

where t is the current time and $\gamma > 0$ is the cooperative coefficient to be designed.

As evident from Eq. (28), the nominal range-to-go is zero during $t = T_d$. If each missile can make its distance to the target track an error within the nominal range-to-go ratio by controlling the rudder angle, then a simultaneous attack can be achieved within a predefined impact time. Hence, the fixed-impact time constraint is transformed into a missile-target distance constraint.

Moreover, we assumed that each missile could attack a target at its predefined azimuth at the interception point by controlling the rudder angle. In this case, it can achieve a multidirectional attack on the target, thereby enhancing the attack efficiency and increasing the damage effect.

If the desired attack azimuth is denoted as q_{2d}, redefining the system states $\mathbf{x}_0 = [R - R_d, q_2 - q_{2d}]^T$ and $\mathbf{x}_1 = [\dot{R} - \dot{R}_d, \dot{q}_2 - \dot{q}_{2d}]^T$, the first and second equations in Eq. (26) can be rewritten as

$$\begin{cases} \dot{\mathbf{x}}_0 = \mathbf{x}_1 \\ \dot{\mathbf{x}}_1 = \mathbf{F}_1 + \mathbf{G}_1 \mathbf{x}_2^* + \mathbf{d}_1 \end{cases}, \tag{29}$$

where

$$\mathbf{F}_1 = \begin{bmatrix} R\dot{q}_1^2 + R\dot{q}_2^2 \cos^2 q_1 + f_{R1} g \cos\theta_M - \ddot{R}_d \\ -\dfrac{2\dot{R}\dot{q}_2}{R} + 2\dot{q}_1\dot{q}_2 \tan q_1 + f_{\eta 1} g \cos\theta_M - \ddot{q}_{2d} \end{bmatrix}^T,$$

391 $$\mathbf{G}_1=\begin{bmatrix} -f_{R1}\dfrac{c_Y^{\alpha}QS}{m} & f_{R2}\dfrac{c_Z^{\beta}QS}{m} \\ -f_{\eta 1}\dfrac{c_Y^{\alpha}QS}{m} & f_{\eta 2}\dfrac{c_Z^{\beta}QS}{m} \end{bmatrix}^T.$$

392 **3.2 Design of IGC controller**

393 In this section, each subsystem is designed based on SMC, DSC, and 3D reduced-
394 order ESO.

395 **Step 1**: For the seeker subsystem, the first sliding mode surface is defined as

396 $$\mathbf{s}_0=\mathbf{x}_0. \tag{30}$$

397 Differentiating Eq. (30), and combining Eq. (29) yields

398 $$\dot{\mathbf{s}}_0=\dot{\mathbf{x}}_0=\mathbf{x}_1. \tag{31}$$

399 Choosing $\mathbf{x}_1$ as the virtual control command that can be designed as follows:

400 $$\mathbf{x}_{1c}=-\mathbf{k}_0\mathbf{s}_0, \tag{32}$$

401 where $\mathbf{k}_0=\mathrm{diag}(k_{01},k_{02})$ is a positive diagonal matrix.

402 The DSC is adopted so that $\mathbf{x}_{1c}$ is passed through a first-order–low-pass filter to
403 obtain $\mathbf{x}_{1d}$ and $\dot{\mathbf{x}}_{1d}$ to avoid the "differential explosion" caused by the BC.

404 $$\begin{cases} \boldsymbol{\tau}_1\dot{\mathbf{x}}_{1d}+\mathbf{x}_{1d}=\mathbf{x}_{1c} \\ \mathbf{x}_{1d}(0)=\mathbf{x}_{1c}(0) \end{cases}, \tag{33}$$

405 where $\boldsymbol{\tau}_1=\mathrm{diag}(\tau_{11},\tau_{12})$ is a filter time constant matrix.

406 **Step 2**: To ensure that the guidance subsystem tracks the virtual control commands of
407 the seeker subsystem, the second sliding mode surface is defined as follows:

408 $$\mathbf{s}_1=\mathbf{x}_1-\mathbf{x}_{1d}. \tag{34}$$

409 Differentiating Eq. (34), and combining Eq. (29) yields

410 $$\begin{aligned} \dot{\mathbf{s}}_1&=\dot{\mathbf{x}}_1-\dot{\mathbf{x}}_{1d} \\ &=\mathbf{F}_1+\mathbf{G}_1\mathbf{x}_2^*+\mathbf{d}_1-\dot{\mathbf{x}}_{1d} \end{aligned}. \tag{35}$$

411 Choosing $\mathbf{x}_2^*$ as the virtual control command that can be designed as follows:

$$\mathbf{x}_{2c}^{*}=\mathbf{G}_1^{-1}\left[-\mathbf{F}_1-\hat{\mathbf{d}}_1+\dot{\mathbf{x}}_{1d}-\mathbf{k}_1\mathbf{s}_1\right], \tag{36}$$

where $\mathbf{k}_1=\mathrm{diag}(k_{11},k_{12})$ is the positive diagonal matrix. $\hat{\mathbf{d}}_1$ is the estimate of $\mathbf{d}_1$, which can be obtained using a 3D reduced-order ESO.

$$\begin{cases}\dot{\mathbf{z}}_1=-\boldsymbol{\beta}_1\mathbf{z}_1-\boldsymbol{\beta}_1^2\mathbf{x}_1-\boldsymbol{\beta}_1\left[\mathbf{F}_1+\mathbf{G}_1\mathbf{x}_2^{*}\right]\\ \hat{\mathbf{d}}_1=\mathbf{z}_1+\boldsymbol{\beta}_1\mathbf{x}_1\end{cases}, \tag{37}$$

where $\mathbf{z}_1=[z_{11},z_{12}]^T$ denotes the auxiliary signal variable vector. $\boldsymbol{\beta}_1=[\beta_{11},\beta_{12}]^T$ is the observer gain diagonal matrix and $\beta_{1i}>0$, which determines the initial estimated error value and error convergence rate.

$\mathbf{x}_{2c}^{*}$ is continuous and has no switching term; thus, the chattering caused by the traditional SMC can be avoided.

$\mathbf{x}_{2d}^{*}$ and $\dot{\mathbf{x}}_{2d}^{*}$ are obtained by passing $\mathbf{x}_{2c}^{*}$ through a first-order–low-pass filter.

$$\begin{cases}\boldsymbol{\tau}_2\dot{\mathbf{x}}_{2d}^{*}+\mathbf{x}_{2d}^{*}=\mathbf{x}_{2c}^{*}\\ \mathbf{x}_{2d}^{*}(0)=\mathbf{x}_{2c}^{*}(0)\end{cases}, \tag{38}$$

where $\boldsymbol{\tau}_2=\mathrm{diag}(\tau_{21},\tau_{22})$ is a filter time constant diagonal matrix.

Step 3: The desired velocity-deflection angle of the missile should be zero to ensure flight stability of the STT missile. Therefore, $\mathbf{x}_{2d}=[\mathbf{x}_{2d}^{*},0]^T$ can define the third sliding mode surface as

$$\mathbf{s}_2=\mathbf{x}_2-\mathbf{x}_{2d}. \tag{39}$$

Differentiating Eq. (39) and combining the third equation in Eq. (26) yields

$$\begin{aligned}\dot{\mathbf{s}}_2&=\dot{\mathbf{x}}_2-\dot{\mathbf{x}}_{2d}\\ &=\mathbf{F}_2+\mathbf{G}_2\mathbf{x}_3+\mathbf{d}_2-\dot{\mathbf{x}}_{2d}\end{aligned}. \tag{40}$$

Choosing $\mathbf{x}_3$ as the virtual control command that can be designed as follows:

$$\mathbf{x}_{3c}=\mathbf{G}_2^{-1}[-\mathbf{F}_2-\hat{\mathbf{d}}_2+\dot{\mathbf{x}}_{2d}-\mathbf{k}_2\mathbf{s}_2], \tag{41}$$

where $\mathbf{k}_2$ is the positive diagonal matrix. $\hat{\mathbf{d}}_2$ is the estimate of $\mathbf{d}_2$, which can be

obtained using a 3D reduced-order ESO.

$$\begin{cases} \dot{\mathbf{z}}_2 = -\boldsymbol{\beta}_2 \mathbf{z}_2 - \boldsymbol{\beta}_2^2 \mathbf{x}_2 - \boldsymbol{\beta}_2 \left[\mathbf{F}_2 + \mathbf{G}_2 \mathbf{x}_3^* \right] \\ \hat{\mathbf{d}}_2 = \mathbf{z}_2 + \boldsymbol{\beta}_2 \mathbf{x}_2 \end{cases}, \tag{42}$$

where $\mathbf{z}_2 = [z_{21}, z_{22}, z_{23}]^T$ denotes the auxiliary signal variable vector. $\boldsymbol{\beta}_2 = [\beta_{21}, \beta_{22}, \beta_{23}]^T$ is the observer gain diagonal matrix, and $\beta_{2i} > 0$.

$\mathbf{x}_{3d}$ and $\dot{\mathbf{x}}_{3d}$ are obtained by passing $\mathbf{x}_{3c}$ through a first-order–low-pass filter.

$$\begin{cases} \boldsymbol{\tau}_3 \dot{\mathbf{x}}_{3d} + \mathbf{x}_{3d} = \mathbf{x}_{3c} \\ \mathbf{x}_{3d}(0) = \mathbf{x}_{3c}(0) \end{cases}, \tag{43}$$

where $\boldsymbol{\tau}_3 = \mathrm{diag}(\tau_{31}, \tau_{32}, \tau_{33})$ is a filter time constant diagonal matrix.

Step 4: To ensure that the attitude subsystem tracks the virtual control commands of the angle-of-attack subsystem, the fourth sliding mode surface is defined as

$$\mathbf{s}_3 = \mathbf{x}_3 - \mathbf{x}_{3d}. \tag{44}$$

Differentiating Eq. (44) and combining the fourth equation in Eq. (26) yields

$$\begin{aligned} \dot{\mathbf{s}}_3 &= \dot{\mathbf{x}}_3 - \dot{\mathbf{x}}_{3d} \\ &= \mathbf{F}_3 + \mathbf{G}_3 \mathbf{x}_4 + \mathbf{d}_3 - \dot{\mathbf{x}}_{3d} \end{aligned}. \tag{45}$$

Choosing $\mathbf{x}_4$ as the virtual control command that can be designed as follows:

$$\mathbf{x}_{4c} = \mathbf{G}_3^{-1} [-\mathbf{F}_3 - \hat{\mathbf{d}}_3 + \dot{\mathbf{x}}_{3d} - \mathbf{k}_3 \mathbf{s}_3], \tag{46}$$

where $\mathbf{k}_3$ is the positive diagonal matrix. $\hat{\mathbf{d}}_3$ is the estimate of $\mathbf{d}_3$, which can be obtained using a 3D reduced-order ESO.

$$\begin{cases} \dot{\mathbf{z}}_3 = -\boldsymbol{\beta}_3 \mathbf{z}_3 - \boldsymbol{\beta}_3^2 \mathbf{x}_3 - \boldsymbol{\beta}_3 \left[\mathbf{F}_3 + \mathbf{G}_3 \mathbf{x}_4^* \right] \\ \hat{\mathbf{d}}_3 = \mathbf{z}_3 + \boldsymbol{\beta}_3 \mathbf{x}_3 \end{cases}, \tag{47}$$

where $\mathbf{z}_3 = [z_{31}, z_{32}, z_{33}]^T$ denotes the auxiliary signal variable vector. $\boldsymbol{\beta}_3 = [\beta_{31}, \beta_{32}, \beta_{33}]^T$ is the observer gain diagonal matrix, and $\beta_{3i} > 0$.

$\mathbf{x}_{4d}$ and $\dot{\mathbf{x}}_{4d}$ are obtained by passing $\mathbf{x}_{4c}$ through a first-order low-pass filter.

$$\begin{cases} \boldsymbol{\tau}_4 \dot{\mathbf{x}}_{4d} + \mathbf{x}_{4d} = \mathbf{x}_{4c} \\ \mathbf{x}_{4d}(0) = \mathbf{x}_{4c}(0) \end{cases}, \tag{48}$$

where $\boldsymbol{\tau}_4 = \mathrm{diag}(\tau_{41}, \tau_{42}, \tau_{43})$ is a filter time constant diagonal matrix.

Step 5: To ensure that the rudder subsystem tracks the virtual control commands of the attitude subsystem, the fifth sliding mode surface is defined as

$$\mathbf{s}_4 = \mathbf{x}_4 - \mathbf{x}_{4d}. \tag{49}$$

Differentiating Eq. (49), and combining Eq. (27) yields

$$\begin{aligned} \dot{\mathbf{s}}_4 &= \dot{\mathbf{x}}_4 - \dot{\mathbf{x}}_{4d} \\ &= \mathbf{F}_4 + \mathbf{G}_4 \mathbf{u} + \mathbf{d}_4 - \dot{\mathbf{x}}_{4d} \end{aligned}. \tag{50}$$

The CIGC control law $\mathbf{u}$ can be designed as follows:

$$\mathbf{u} = \mathbf{G}_4^{-1}[-\mathbf{F}_4 - \hat{\mathbf{d}}_4 + \dot{\mathbf{x}}_{4d} - \mathbf{k}_4 \mathbf{s}_4], \tag{51}$$

where $\mathbf{k}_4$ is the positive diagonal matrix. $\hat{\mathbf{d}}_4$ is the estimate of $\mathbf{d}_4$, which can be obtained using a 3D reduced-order ESO.

$$\begin{cases} \dot{\mathbf{z}}_4 = -\boldsymbol{\beta}_4 \mathbf{z}_4 - \boldsymbol{\beta}_4^2 \mathbf{x}_4 - \boldsymbol{\beta}_4 \left[\mathbf{F}_4 + \mathbf{G}_4 \mathbf{u} \right] \\ \hat{\mathbf{d}}_4 = \mathbf{z}_4 + \boldsymbol{\beta}_4 \mathbf{x}_4 \end{cases}, \tag{52}$$

where $\mathbf{z}_4 = [z_{41}, z_{42}, z_{43}]^T$ denotes the auxiliary signal variable vector. $\boldsymbol{\beta}_4 = [\beta_{41}, \beta_{42}, \beta_{43}]^T$ is the observer gain diagonal matrix, and $\beta_{4i} > 0$.

Finally, the proposed control law includes virtual control commands, which can be summarized as follows:

$$
\begin{cases}
\mathbf{s}_0 = \mathbf{x}_0 \\
\mathbf{x}_{1c} = -\mathbf{k}_0 \mathbf{s}_0 \\
\boldsymbol{\tau}_1 \dot{\mathbf{x}}_{1d} + \mathbf{x}_{1d} = \mathbf{x}_{1c}, \mathbf{x}_{1d}(0) = \mathbf{x}_{1c}(0) \\
\mathbf{s}_1 = \mathbf{x}_1 - \mathbf{x}_{1d} \\
\mathbf{x}_{2c}^* = \mathbf{G}_1^{-1}[-\mathbf{F}_1 - \hat{\mathbf{d}}_1 + \dot{\mathbf{x}}_{1d} - \mathbf{k}_1 \mathbf{s}_1] \\
\boldsymbol{\tau}_2 \dot{\mathbf{x}}_{2d}^* + \mathbf{x}_{2d}^* = \mathbf{x}_{2c}^*, \mathbf{x}_{2d}^*(0) = \mathbf{x}_{2c}^*(0) \\
\mathbf{x}_{2d} = [\dot{\mathbf{x}}_{2d}^*, 0]^T \\
\mathbf{s}_2 = \mathbf{x}_2 - \mathbf{x}_{2d} \\
\mathbf{x}_{3c} = \mathbf{G}_2^{-1}[-\mathbf{F}_2 - \hat{\mathbf{d}}_2 + \dot{\mathbf{x}}_{2d} - \mathbf{k}_2 \mathbf{s}_2] \\
\boldsymbol{\tau}_3 \dot{\mathbf{x}}_{3d} + \mathbf{x}_{3d} = \mathbf{x}_{3c}, \mathbf{x}_{3d}(0) = \mathbf{x}_{3c}(0) \\
\mathbf{s}_3 = \mathbf{x}_3 - \mathbf{x}_{3d} \\
\mathbf{x}_{4c} = \mathbf{G}_3^{-1}[-\mathbf{F}_3 - \hat{\mathbf{d}}_3 + \dot{\mathbf{x}}_{3d} - \mathbf{k}_3 \mathbf{s}_3] \\
\boldsymbol{\tau}_4 \dot{\mathbf{x}}_{4d} + \mathbf{x}_{4d} = \mathbf{x}_{4c}, \mathbf{x}_{4d}(0) = \mathbf{x}_{4c}(0) \\
\mathbf{s}_4 = \mathbf{x}_4 - \mathbf{x}_{4d} \\
\mathbf{u} = \mathbf{G}_4^{-1}[-\mathbf{F}_4 - \hat{\mathbf{d}}_4 + \dot{\mathbf{x}}_{4d} - \mathbf{k}_4 \mathbf{s}_4]
\end{cases}
. \tag{53}
$$

4. Stability analysis

For the 3D nonlinear strict-feedback IGC model, Eqs. (26) and (27) and the proposed CIGC scheme in Eq. (53), the stability of the closed-loop system is proved using Lyapunov theory.

Theorem. 1. Based on the proposed CIGC scheme, Eq. (53), and the 3D reduced-order ESO for the proposed 3D strict-feedback nonlinear IGC model in Eqs. (26) and (27) with mismatched uncertainties, the closed-loop system stability can be ensured by adjusting the controller parameters, observer gains, and filter time constants.

Assumption. 6. The estimation error $\left\|\mathbf{d}_i-\hat{\mathbf{d}}_i\right\|<m_i, i=1,2,3,4$ (m_i is a positive constant) can be guaranteed using the 3D reduced-order ESO estimation system-lumped disturbance $\mathbf{d}_i, i=1,2,3,4$. Furthermore, the observer estimation errors can converge to an arbitrarily small range by adjusting the observer gains.[32]

The filter tracking errors can be defined as

$$\begin{cases}\mathbf{e}_1=\mathbf{x}_{1d}-\mathbf{x}_{1c}\\ \mathbf{e}_2=\mathbf{x}_{2d}^*-\mathbf{x}_{2c}^*\\ \mathbf{e}_3=\mathbf{x}_{3d}-\mathbf{x}_{3c}\\ \mathbf{e}_4=\mathbf{x}_{4d}-\mathbf{x}_{4c}\end{cases}. \tag{54}$$

Differentiating Eq. (54) gives

$$\begin{cases}\dot{\mathbf{e}}_1=-\boldsymbol{\tau}_1^{-1}\mathbf{e}_1-\dot{\mathbf{x}}_{1c}\\ \dot{\mathbf{e}}_2=-\boldsymbol{\tau}_2^{-1}\mathbf{e}_2-\dot{\mathbf{x}}_{2c}^*\\ \dot{\mathbf{e}}_3=-\boldsymbol{\tau}_3^{-1}\mathbf{e}_3-\dot{\mathbf{x}}_{3c}\\ \dot{\mathbf{e}}_4=-\boldsymbol{\tau}_4^{-1}\mathbf{e}_4-\dot{\mathbf{x}}_{4c}\end{cases}. \tag{55}$$

Equation (55) is calculated by simple algebra to obtain

$$\mathbf{e}_1^T\dot{\mathbf{e}}_1=-\mathbf{e}_1^T\boldsymbol{\tau}_1^{-1}\mathbf{e}_1-\mathbf{e}_1^T\dot{\mathbf{x}}_{1c}\le-\mathbf{e}_1^T\left(\boldsymbol{\tau}_1^{-1}-\frac{1}{2}\left\|\dot{\mathbf{x}}_{1c}\right\|^2\mathbf{I}_2\right)\mathbf{e}_1+\frac{1}{2}, \tag{56}$$

$$\mathbf{e}_2^T\dot{\mathbf{e}}_2=-\mathbf{e}_2^T\boldsymbol{\tau}_2^{-1}\mathbf{e}_2-\mathbf{e}_2^T\dot{\mathbf{x}}_{2c}\le-\mathbf{e}_2^T\left(\boldsymbol{\tau}_2^{-1}-\frac{1}{2}\left\|\dot{\mathbf{x}}_{2c}^*\right\|^2\mathbf{I}_2\right)\mathbf{e}_2+\frac{1}{2}, \tag{57}$$

$$\mathbf{e}_3^T\dot{\mathbf{e}}_3=-\mathbf{e}_3^T\boldsymbol{\tau}_3^{-1}\mathbf{e}_3-\mathbf{e}_3^T\dot{\mathbf{x}}_{3c}\le-\mathbf{e}_3^T\left(\boldsymbol{\tau}_3^{-1}-\frac{1}{2}\left\|\dot{\mathbf{x}}_{3c}\right\|^2\mathbf{I}_3\right)\mathbf{e}_3+\frac{1}{2}, \tag{58}$$

$$\mathbf{e}_4^T\dot{\mathbf{e}}_4 = -\mathbf{e}_4^T\boldsymbol{\tau}_4^{-1}\mathbf{e}_4 - \mathbf{e}_4^T\dot{\mathbf{x}}_{4c} \le -\mathbf{e}_4^T\left(\boldsymbol{\tau}_4^{-1} - \frac{1}{2}\left\|\dot{\mathbf{x}}_{4c}\right\|^2\mathbf{I}_3\right)\mathbf{e}_4 + \frac{1}{2}, \tag{59}$$

where $\mathbf{I}_2$ and $\mathbf{I}_3$ denote identity matrix.

We let the Lyapunov function candidate be

$$V_s = V_0 + V_1 + V_2 + V_3 + V_4, \tag{60}$$

where

$$V_0 = \frac{1}{2}\mathbf{s}_0^T\mathbf{s}_0, \tag{61}$$

$$V_1 = \frac{1}{2}\mathbf{s}_1^T\mathbf{s}_1 + \frac{1}{2}\mathbf{e}_1^T\mathbf{e}_1, \tag{62}$$

$$V_2 = \frac{1}{2}\mathbf{s}_2^T\mathbf{s}_2 + \frac{1}{2}\mathbf{e}_2^T\mathbf{e}_2, \tag{63}$$

$$V_3 = \frac{1}{2}\mathbf{s}_3^T\mathbf{s}_3 + \frac{1}{2}\mathbf{e}_3^T\mathbf{e}_3, \tag{64}$$

$$V_4 = \frac{1}{2}\mathbf{s}_4^T\mathbf{s}_4 + \frac{1}{2}\mathbf{e}_4^T\mathbf{e}_4. \tag{65}$$

Combining Eqs. (53)–(55), after some algebraic computations, we have

$$\begin{aligned}\mathbf{s}_0^T\dot{\mathbf{s}}_0 &= \mathbf{s}_0^T\dot{\mathbf{x}}_0 = \mathbf{s}_0^T\mathbf{x}_1\\ &= \mathbf{s}_0^T\left(\mathbf{s}_1 + \mathbf{e}_1 + \mathbf{x}_{1c}\right)\\ &= \mathbf{s}_0^T\left(\mathbf{s}_1 + \mathbf{e}_1 - \mathbf{k}_0\mathbf{s}_0\right)\\ &\le -\mathbf{s}_0^T\left[\mathbf{k}_0 - \frac{1}{2}\mathbf{I}_2\right]\mathbf{s}_0 + \mathbf{s}_1^T\mathbf{s}_1 + \mathbf{e}_1^T\mathbf{e}_1\end{aligned}, \tag{66}$$

$$\begin{aligned}\mathbf{s}_1^T\dot{\mathbf{s}}_1 &= \mathbf{s}_1^T\left(\dot{\mathbf{x}}_1 - \dot{\mathbf{x}}_{1d}\right) = \mathbf{s}_1^T\left(\mathbf{F}_1 + \mathbf{G}_1\mathbf{x}_2^* + \mathbf{d}_1 - \dot{\mathbf{x}}_{1d}\right)\\ &= \mathbf{s}_1^T\left[\mathbf{F}_1 + \mathbf{G}_1\left(\mathbf{s}_2^* + \mathbf{e}_2 + \mathbf{x}_{2c}^*\right) + \mathbf{d}_1 - \dot{\mathbf{x}}_{1d}\right]\\ &= \mathbf{s}_1^T\mathbf{G}_1\left(\mathbf{s}_2^* + \mathbf{e}_2\right) + \mathbf{s}_1^T\left(\mathbf{d}_1 - \hat{\mathbf{d}}_1\right) - \mathbf{s}_1^T\mathbf{k}_1\mathbf{s}_1\\ &\le -\mathbf{s}_1^T\left[\mathbf{k}_1 - \frac{1}{2}\mathbf{G}_1^2 - \frac{1}{4}\mathbf{I}_2\right]\mathbf{s}_1 + \mathbf{s}_2^T\mathbf{s}_2 + \mathbf{e}_2^T\mathbf{e}_2 + m_1^2\end{aligned}, \tag{67}$$

$$\begin{aligned}\mathbf{s}_2^T\dot{\mathbf{s}}_2 &= \mathbf{s}_2^T\left(\dot{\mathbf{x}}_2 - \dot{\mathbf{x}}_{2d}\right) = \mathbf{s}_2^T\left(\mathbf{F}_2 + \mathbf{G}_2\mathbf{x}_3 + \mathbf{d}_2 - \dot{\mathbf{x}}_{2d}\right)\\ &= \mathbf{s}_2^T\left[\mathbf{F}_2 + \mathbf{G}_2\left(\mathbf{s}_3 + \mathbf{e}_3 + \mathbf{x}_{3c}\right) + \mathbf{d}_2 - \dot{\mathbf{x}}_{2d}\right]\\ &= \mathbf{s}_2^T\mathbf{G}_2\left(\mathbf{s}_3 + \mathbf{e}_3\right) + \mathbf{s}_2^T\left(\mathbf{d}_2 - \hat{\mathbf{d}}_2\right) - \mathbf{s}_2^T\mathbf{k}_2\mathbf{s}_2\\ &\le -\mathbf{s}_2^T\left[\mathbf{k}_2 - \frac{1}{2}\mathbf{G}_2^2 - \frac{1}{4}\mathbf{I}_3\right]\mathbf{s}_2 + \mathbf{s}_3^T\mathbf{s}_3 + \mathbf{e}_3^T\mathbf{e}_3 + m_2^2\end{aligned}, \tag{68}$$

$$\begin{aligned}\mathbf{s}_3^T\dot{\mathbf{s}}_3 &= \mathbf{s}_3^T\left(\dot{\mathbf{x}}_3-\dot{\mathbf{x}}_{3d}\right)=\mathbf{s}_3^T\left(\mathbf{F}_3+\mathbf{G}_3\mathbf{x}_4+\mathbf{d}_3-\dot{\mathbf{x}}_{3d}\right)\\ &=\mathbf{s}_3^T\left[\mathbf{F}_3+\mathbf{G}_3\left(\mathbf{s}_4+\mathbf{e}_4+\mathbf{x}_{4c}\right)+\mathbf{d}_3-\dot{\mathbf{x}}_{3d}\right]\\ &=\mathbf{s}_3^T\mathbf{G}_3\left(\mathbf{s}_4+\mathbf{e}_4\right)+\mathbf{s}_3^T\left(\mathbf{d}_3-\hat{\mathbf{d}}_3\right)-\mathbf{s}_3^T\mathbf{k}_3\mathbf{s}_3\\ &\le -\mathbf{s}_3^T\left[\mathbf{k}_3-\frac{1}{2}\mathbf{G}_3^2-\frac{1}{4}\mathbf{I}_3\right]\mathbf{s}_3+\mathbf{s}_4^T\mathbf{s}_4+\mathbf{e}_4^T\mathbf{e}_4+m_3^2\end{aligned}, \tag{69}$$

$$\begin{aligned}\mathbf{s}_4^T\dot{\mathbf{s}}_4 &= \mathbf{s}_4^T\left(\dot{\mathbf{x}}_4-\dot{\mathbf{x}}_{4d}\right)=\mathbf{s}_4^T\left(\mathbf{F}_4+\mathbf{G}_4\mathbf{u}+\mathbf{d}_4-\dot{\mathbf{x}}_{4d}\right)\\ &=\mathbf{s}_4^T\left[\mathbf{d}_4-\hat{\mathbf{d}}_4-\mathbf{k}_4\mathbf{s}_4\right]\\ &\le -\mathbf{s}_4^T\left[\mathbf{k}_4-\frac{1}{4}\mathbf{I}_3\right]\mathbf{s}_4+m_4^2\end{aligned}. \tag{70}$$

Differentiating Eqs. (61)–(65) and combining Eqs. (56)–(59) and (66)–(70) yields

$$\dot{V}_0=\mathbf{s}_0^T\dot{\mathbf{s}}_0\le -\mathbf{s}_0^T\left[\mathbf{k}_0-\frac{1}{2}\mathbf{I}_2\right]\mathbf{s}_0+\mathbf{s}_1^T\mathbf{s}_1+\mathbf{e}_1^T\mathbf{e}_1, \tag{71}$$

$$\begin{aligned}\dot{V}_1 &= \mathbf{s}_1^T\dot{\mathbf{s}}_1+\mathbf{e}_1^T\dot{\mathbf{e}}_1\\ &\le -\mathbf{s}_1^T\left[\mathbf{k}_1-\frac{1}{2}\mathbf{G}_1^2-\frac{1}{4}\mathbf{I}_2\right]\mathbf{s}_1+\mathbf{s}_2^T\mathbf{s}_2+\mathbf{e}_2^T\mathbf{e}_2+m_1^2-\mathbf{e}_1^T\left(\boldsymbol{\tau}_1^{-1}-\frac{1}{2}\left\|\dot{\mathbf{x}}_{1c}\right\|^2\mathbf{I}_2\right)\mathbf{e}_1+\frac{1}{2}\end{aligned}, \tag{72}$$

$$\begin{aligned}\dot{V}_2 &= \mathbf{s}_2^T\dot{\mathbf{s}}_2+\mathbf{e}_2^T\dot{\mathbf{e}}_2\\ &\le -\mathbf{s}_2^T\left[\mathbf{k}_2-\frac{1}{2}\mathbf{G}_2^2-\frac{1}{4}\mathbf{I}_3\right]\mathbf{s}_2+\mathbf{s}_3^T\mathbf{s}_3+\mathbf{e}_3^T\mathbf{e}_3+m_2^2-\mathbf{e}_2^T\left(\boldsymbol{\tau}_2^{-1}-\frac{1}{2}\left\|\dot{\mathbf{x}}_{2c}^*\right\|^2\mathbf{I}_2\right)\mathbf{e}_2+\frac{1}{2}\end{aligned}, \tag{73}$$

$$\begin{aligned}\dot{V}_3 &= \mathbf{s}_3^T\dot{\mathbf{s}}_3+\mathbf{e}_3^T\dot{\mathbf{e}}_3\\ &\le -\mathbf{s}_3^T\left[\mathbf{k}_3-\frac{1}{2}\mathbf{G}_3^2-\frac{1}{4}\mathbf{I}_3\right]\mathbf{s}_3+\mathbf{s}_4^T\mathbf{s}_4+\mathbf{e}_4^T\mathbf{e}_4+m_3^2-\mathbf{e}_3^T\left(\boldsymbol{\tau}_3^{-1}-\frac{1}{2}\left\|\dot{\mathbf{x}}_{3c}\right\|^2\mathbf{I}_3\right)\mathbf{e}_3+\frac{1}{2}\end{aligned}, \tag{74}$$

$$\begin{aligned}\dot{V}_4 &= \mathbf{s}_4^T\dot{\mathbf{s}}_4+\mathbf{e}_4^T\dot{\mathbf{e}}_4\\ &\le -\mathbf{s}_4^T\left[\mathbf{k}_4-\frac{1}{4}\mathbf{I}_3\right]\mathbf{s}_4+m_4^2-\mathbf{e}_4^T\left(\boldsymbol{\tau}_4^{-1}-\frac{1}{2}\left\|\dot{\mathbf{x}}_{4c}\right\|^2\mathbf{I}_3\right)\mathbf{e}_4+\frac{1}{2}\end{aligned}. \tag{75}$$

Differentiating Eq. (60), and combining Eqs. (71)–(75) yields

$$
\begin{aligned}
\dot{V}_s &= \dot{V}_0 + \dot{V}_1 + \dot{V}_2 + \dot{V}_3 + \dot{V}_4 \\
&\le -\mathbf{s}_0^T\left[\mathbf{k}_0 - \frac{1}{2}\mathbf{I}_2\right]\mathbf{s}_0 - \mathbf{s}_1^T\left[\mathbf{k}_1 - \frac{1}{2}\mathbf{G}_1^2 - \frac{5}{4}\mathbf{I}_2\right]\mathbf{s}_1 - \mathbf{s}_2^T\left[\mathbf{k}_2 - \frac{1}{2}\mathbf{G}_2^2 - \frac{5}{4}\mathbf{I}_3\right]\mathbf{s}_2 \\
&\quad - \mathbf{s}_3^T\left[\mathbf{k}_3 - \frac{1}{2}\mathbf{G}_3^2 - \frac{5}{4}\mathbf{I}_3\right]\mathbf{s}_3 - \mathbf{s}_4^T\left[\mathbf{k}_4 - \frac{5}{4}\mathbf{I}_3\right]\mathbf{s}_4 - \mathbf{e}_1^T\left(\boldsymbol{\tau}_1^{-1} - \frac{1}{2}\left\|\dot{\mathbf{x}}_{1c}\right\|^2\mathbf{I}_2 - \mathbf{I}_2\right)\mathbf{e}_1 \\
&\quad - \mathbf{e}_2^T\left(\boldsymbol{\tau}_2^{-1} - \frac{1}{2}\left\|\dot{\mathbf{x}}_{2c}^*\right\|^2\mathbf{I}_2 - \mathbf{I}_2\right)\mathbf{e}_2 - \mathbf{e}_3^T\left(\boldsymbol{\tau}_3^{-1} - \frac{1}{2}\left\|\dot{\mathbf{x}}_{3c}\right\|^2\mathbf{I}_3 - \mathbf{I}_3\right)\mathbf{e}_3 \\
&\quad - \mathbf{e}_4^T\left(\boldsymbol{\tau}_4^{-1} - \frac{1}{2}\left\|\dot{\mathbf{x}}_{4c}\right\|^2\mathbf{I}_3 - \mathbf{I}_3\right)\mathbf{e}_4 + m_1^2 + m_2^2 + m_3^2 + m_4^2 + 2
\end{aligned} \tag{76}
$$

The appropriate control law parameters and filter parameters are selected, such that

$$
\begin{cases}
\mathbf{k}_0 - \frac{1}{2}\mathbf{I}_2 \ge \frac{1}{2}\kappa\mathbf{I}_2 \\
\mathbf{k}_1 - \frac{1}{2}\mathbf{G}_1^2 - \frac{5}{4}\mathbf{I}_2 \ge \frac{1}{2}\kappa\mathbf{I}_2 \\
\mathbf{k}_2 - \frac{1}{2}\mathbf{G}_2^2 - \frac{5}{4}\mathbf{I}_3 \ge \frac{1}{2}\kappa\mathbf{I}_3 \\
\mathbf{k}_3 - \frac{1}{2}\mathbf{G}_3^2 - \frac{5}{4}\mathbf{I}_3 \ge \frac{1}{2}\kappa\mathbf{I}_3 \\
\mathbf{k}_4 - \frac{5}{4}\mathbf{I}_3 \ge \frac{1}{2}\kappa\mathbf{I}_3 \\
\boldsymbol{\tau}_1^{-1} - \frac{1}{2}\left\|\dot{\mathbf{x}}_{1c}\right\|^2\mathbf{I}_2 - \mathbf{I}_2 \ge \frac{1}{2}\kappa\mathbf{I}_2 \\
\boldsymbol{\tau}_2^{-1} - \frac{1}{2}\left\|\dot{\mathbf{x}}_{2c}^*\right\|^2\mathbf{I}_2 - \mathbf{I}_2 \ge \frac{1}{2}\kappa\mathbf{I}_2 \\
\boldsymbol{\tau}_3^{-1} - \frac{1}{2}\left\|\dot{\mathbf{x}}_{3c}\right\|^2\mathbf{I}_3 - \mathbf{I}_3 \ge \frac{1}{2}\kappa\mathbf{I}_3 \\
\boldsymbol{\tau}_4^{-1} - \frac{1}{2}\left\|\dot{\mathbf{x}}_{4c}\right\|^2\mathbf{I}_3 - \mathbf{I}_3 \ge \frac{1}{2}\kappa\mathbf{I}_3 .
\end{cases} \tag{77}
$$

We define $\eta = m_1^2 + m_2^2 + m_3^2 + m_4^2 + 2$; therefore, Eq. (77) can be rewritten as

$$
\dot{V}_s \le -\kappa V_s + \eta . \tag{78}
$$

According to Eq. (78), we can obtain [33]

$$
0 \le V_s(t) \le \left(V_s(0) - \frac{\eta}{\kappa}\right)e^{-\kappa t} + \frac{\eta}{\kappa} . \tag{79}
$$

It is evident from Eq. (79) that V_s is bounded. It is also proven that the closed-loop system is stable, and the system states are ultimately uniformly bounded.

Remark. 3. For the proposed IGC and CIGC schemes, the closed-loop system is stable and the system states are ultimately uniformly bounded. It can also ensure that the missile-target distance R of all the missiles can accurately track the nominal range-to-go R_d until they hit the target to achieve a simultaneous attack at a predefined impact time T_d. The terminal-impact azimuth q_{2f} can also converge to a predefined impact azimuth q_{2d}. Thus, multiple missiles can simultaneously attack the targets at different azimuths.

Hereto, **Theorem. 1** is proved.

5. Simulations

To verify the effectiveness and robustness of the proposed CIGC scheme, six-degrees-of-freedom (6DOF) numerical simulations were performed.

Table 1 Missile-related parameters

Name	Value	Name	Value	Name	Value
m	1,200 kg	c_y^{β}	−0.081	m_y^{β}	−27.30
S	0.43 m^2	$c_y^{\delta_z}$	5.75	$m_y^{\delta_y}$	−26.60
L	0.69 m	c_z^{α}	0.091	m_z^{α}	−28.15
J_x	100 kg·m^2	c_z^{β}	−56.32	$m_z^{\delta_z}$	−27.90
J_y	5,800 kg·m^2	$c_z^{\delta_y}$	−5.6	τ_x	0.1
J_z	5,700 kg·m^2	m_x^{α}	0.45	τ_y	0.1
ρ	1.1558 kg/m^3	m_x^{β}	−0.38	τ_z	0.1
c_y^{α}	57.15	$m_x^{\delta_x}$	2.13		

Assuming that the STT missiles engaged in the attack are of the same type, the missile body parameters and aerodynamic coefficients are listed in Table 1. It should be noted that the aerodynamic forces from Eq. (17), can be approximated. The aerodynamic forces used in the simulation were as follows:

$$\begin{cases} Y = QS\left(c_y^{\alpha}\alpha + c_y^{\beta}\beta + c_y^{\delta_z}\delta_z\right) \\ Z = QS\left(c_z^{\alpha}\alpha + c_z^{\beta}\beta + c_z^{\delta_y}\delta_y\right) \end{cases}. \tag{80}$$

The parameters of the proposed CIGC scheme are selected as follows:

$\mathbf{k}_0 = \mathrm{diag}(1,1)$, $\mathbf{k}_1 = \mathrm{diag}(35,36)$, $\mathbf{k}_2 = \mathrm{diag}(20,18,18)$, $\mathbf{k}_3 = \mathrm{diag}(10,12,11)$, and $\mathbf{k}_4 = \mathrm{diag}(8,12,12)$.

The time constants of the filter are selected as

$\boldsymbol{\tau}_1 = \mathrm{diag}(0.01,0.01)$, $\boldsymbol{\tau}_2 = \mathrm{diag}(0.001,0.001)$, $\boldsymbol{\tau}_3 = \mathrm{diag}(0.001,0.001,0.001)$, and $\boldsymbol{\tau}_4 = \mathrm{diag}(0.001,0.001,0.001)$.

The 3D reduced-order ESO gain coefficients are selected as

549 $\boldsymbol{\beta}_1 = \mathrm{diag}(10,10)$, $\boldsymbol{\beta}_2 = \mathrm{diag}(15,25,25)$, $\boldsymbol{\beta}_3 = \mathrm{diag}(10,20,20)$, and $\boldsymbol{\beta}_4 = \mathrm{diag}(10,20,20)$.

550 The center-of-mass motion models of the missile and target are expressed in Eq.
551 (81). The guidance states R, q_1, and q_2 were calculated using Eq. (82).

552
$$\begin{cases} \dot{x} = V\cos\theta\cos\psi_V \\ \dot{y} = V\sin\theta \\ \dot{z} = -V\cos\theta\sin\psi_V \end{cases} \tag{81}$$

553
$$\begin{cases} R = \sqrt{(x_t - x_m)^2 + (y_t - y_m)^2 + (z_t - z_m)^2} \\ q_1 = \arctan\left((y_t - y_m)/\sqrt{(x_t - x_m)^2 + (z_t - z_m)^2}\right) \\ q_2 = -\arctan\left((z_t - z_m)/(x_t - x_m)\right) \end{cases} \tag{82}$$

554 The three missiles were assumed to be located at a certain distance from each
555 other at the same height, with the same flight path and heading angles as those in the
556 terminal guidance phase. The initial conditions of the missiles and the desired impact
557 azimuths are listed in Table 2. Because the velocity of a hypersonic missile is
558 significantly greater than that of a ground-moving target, a cooperative strategy
559 coefficient can be designed by treating the target as stationary. The desired impact time
560 is set to $T_d = 5$ s. The cooperative strategy coefficient is set to $\gamma = 1.0$, based on the
561 maximum initial missile-target distance.

562 **Table 2**. Initial conditions for the three missiles

	(x_{m0}, y_{m0}, z_{m0}) (km)	V_M (m/s)	θ_{M0} (°)	ψ_{VM0} (°)	q_{2d} (°)
Missile A	(4.0,6.0,6.0)	2,000	−10	135	115
Missile B	(4.5,6.0,5.5)	2,000	−10	135	135
Missile C	(5.0,6.0,4.0)	2,000	−10	135	160

563 A seeker has a dead zone when it is sufficiently close to the target. The guidance
564 control system cannot operate correctly at this point because it fails to detect the
565 relative motion of the missile-target. Therefore, it can be assumed that the rudder
566 angles did not change. This simulation assumed that the dead-zone radius of the seeker
567 was 30 m. The maximum rudder angle is $\delta_x^{\max} = \delta_y^{\max} = \delta_z^{\max} = 30°$.

Case 1 *Ground fixed target*

The effectiveness of the proposed CIGC scheme was verified by simultaneously attacking a stationary ground target using three missiles. The initial position of the target is determined using $(x_{t0}, y_{t0}, z_{t0}) = (0,0,0)$. Suppose that the coefficients of both aerodynamic forces and moments are reduced by 20% of their respective nominal values. The simulation results are summarized in Table 3 and Figs. 3–9.

Table 3 Simulation results for Case 1.

	T_d (s)	Impact time t_f (s)	q_{2d} (°)	q_{2f} (°)	Miss distance (m)
Missile A	5	4.999	115	115.01	0.1521
Missile B	5	4.999	135	135.03	0.4871
Missile C	5	4.999	160	160.06	0.8867

As shown in Fig. 3 and Table 3, all three missiles could accurately attack a stationary ground target with miss distances of less than 1 m, errors of 1 ms between the actual impact time and predefined impact time, and errors of the terminal-impact azimuth of less than 1°. This confirms the effectiveness of the proposed scheme in the presence of system-lumped disturbances. Figure 4 shows that the missile-target distance of the three missiles can quickly converge to the nominal missile-target range-to-go and subsequently track it until they hit the target. The errors between the actual and predefined impact times satisfy the design requirements. This indicates that the cooperative strategy for transforming the predefined impact time into the desired range using Eq. (28) is effective. Figure 5 shows that the azimuths of the three missiles converge to the desired azimuths, confirming that the designed CIGC scheme can satisfy the desired impact azimuth.

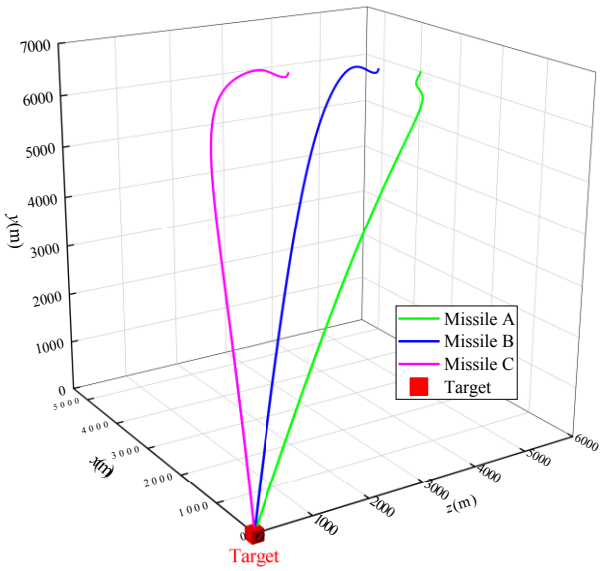

587

588 **Fig. 3.** Trajectories of the three missiles in Case 1.

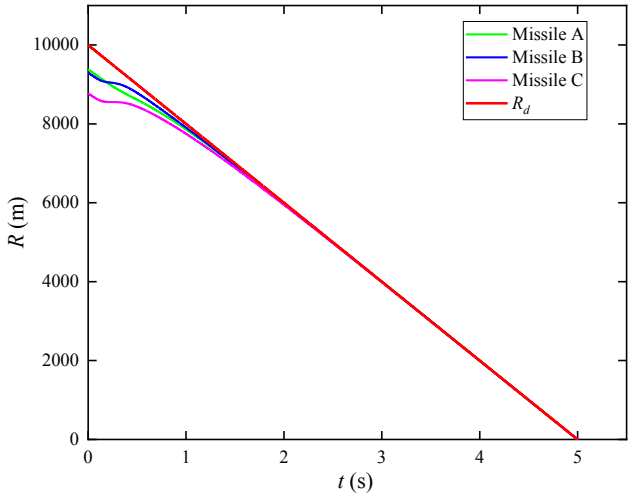

589

590 **Fig. 4.** The three missile-target distance variation curves and nominal ranges follow those

591 of case 1.

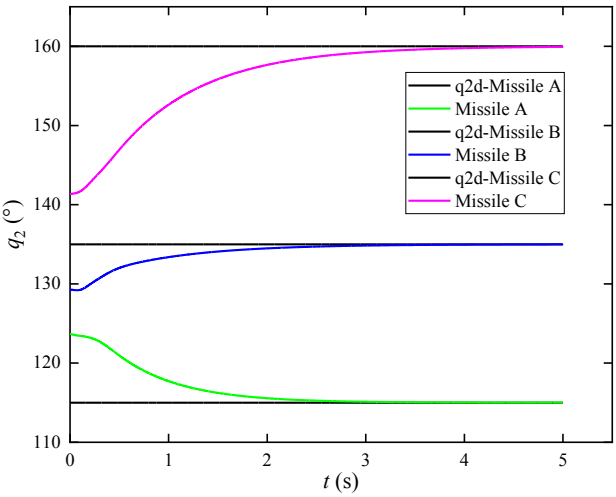

592

Fig. 5. Azimuth curves of the three missiles under Case 1.

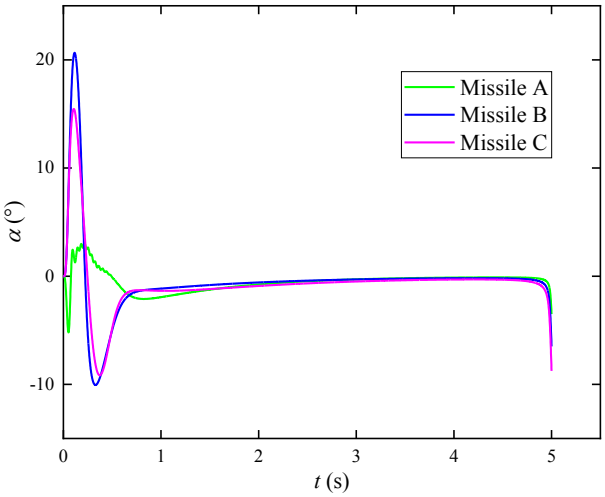

(a)

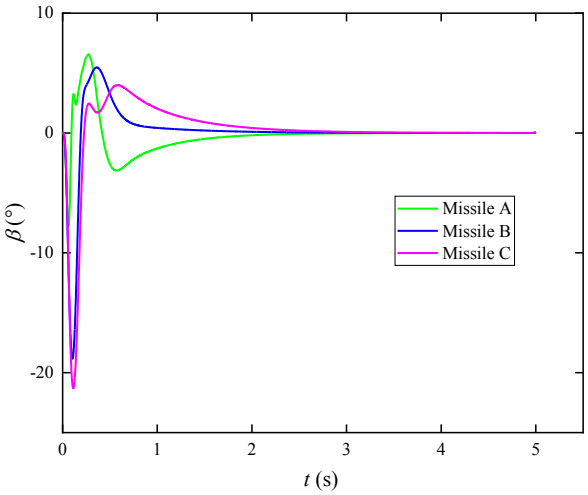

(b)

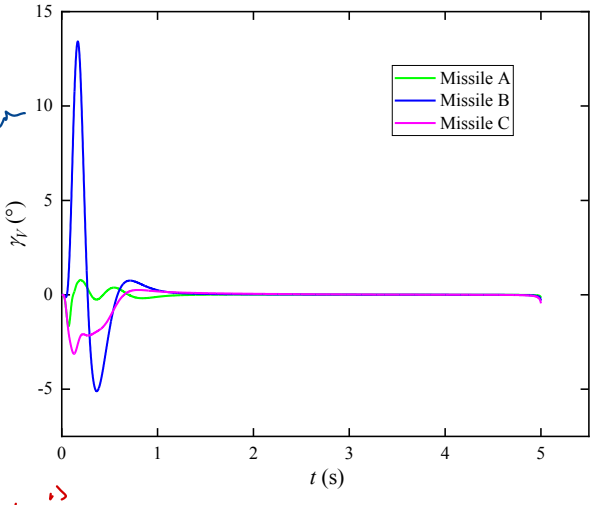

(c)

Fig. 6. Curves of α, β, and γ_V for three missiles in Case 1.

The proposed CIGC scheme assumes a small velocity-deflection angle. In other words, when the velocity-deflection angle is not zero, the errors caused by the approximation can be regarded as unmodeled parts of the system. Figure 6 (c) shows that the velocity-deflection angles of the three missiles oscillate temporarily at the beginning, converge quickly to near zero, and remain there. This indicates that the missiles can still hit the target accurately when the velocity-deflection angle deviates from zero, further demonstrating that the proposed CIGC scheme is effective despite uncertainties. As shown in Figs. 6 (b) and (c), the angle-of-attack and sideslip angle of the three missiles initially show short-term oscillations because the missiles need to adjust their attitudes to meet the desired missile-target distances and azimuths.

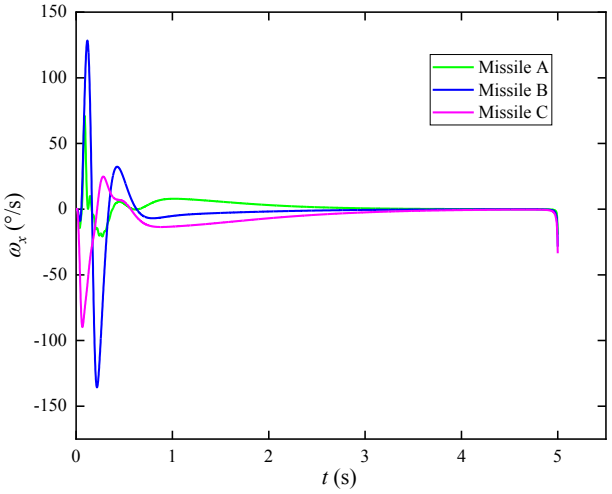

（a）

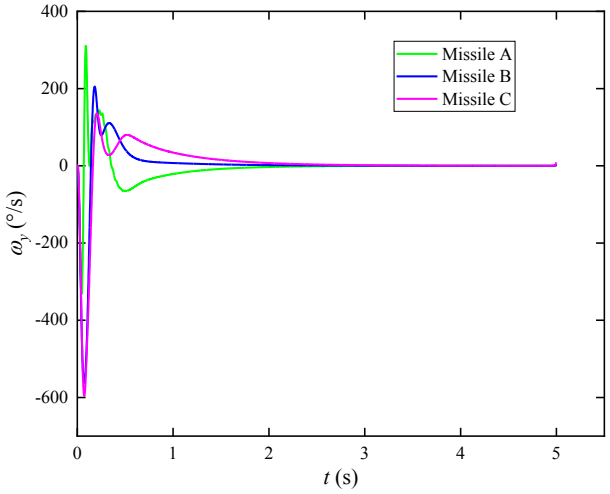

（b）

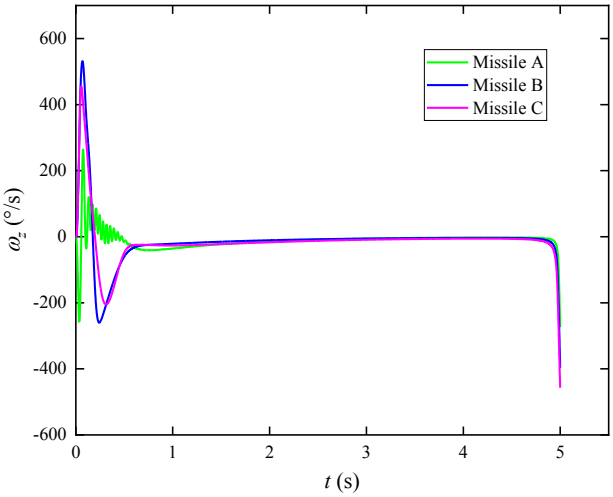

(c)

Fig. 7. Curves of angular rates ω_x, ω_y, and ω_z of three missiles in Case 1.

It can be observed from Fig. 7 that the three angular rates also oscillate briefly at the beginning to satisfy the initial attitude adjustments of the missiles and then remain stable. Figure 8 shows that the rudder angles of the three missiles did not exceed the maximum rudder angle.

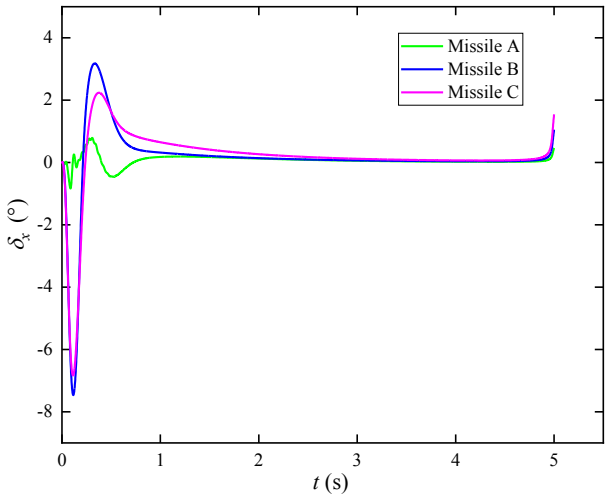

(a)

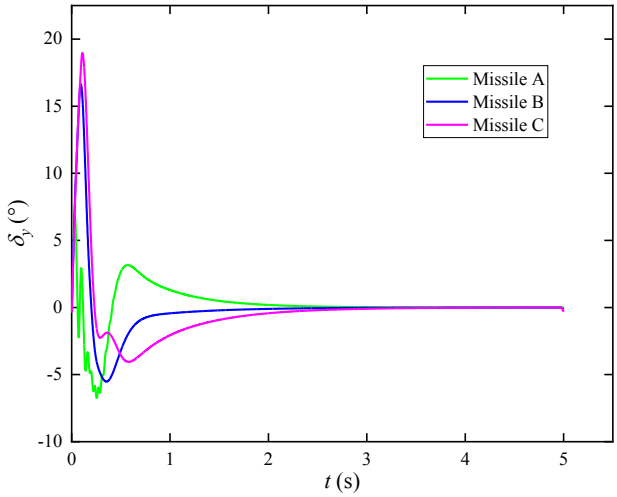

(b)

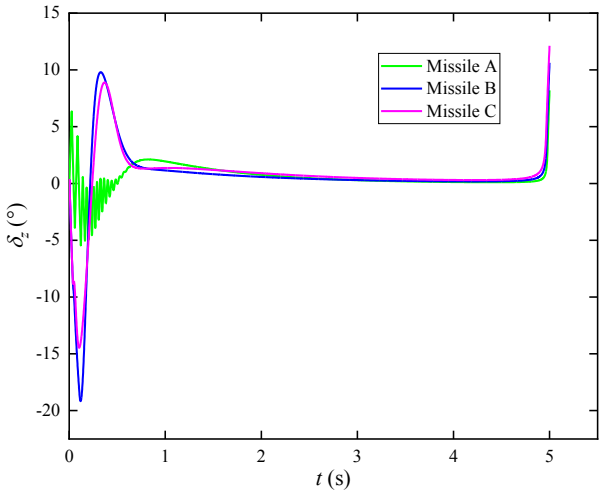

(c)

Fig. 8. Curves of rudder angles δ_x, δ_y, and δ_z for three missiles in Case 1.

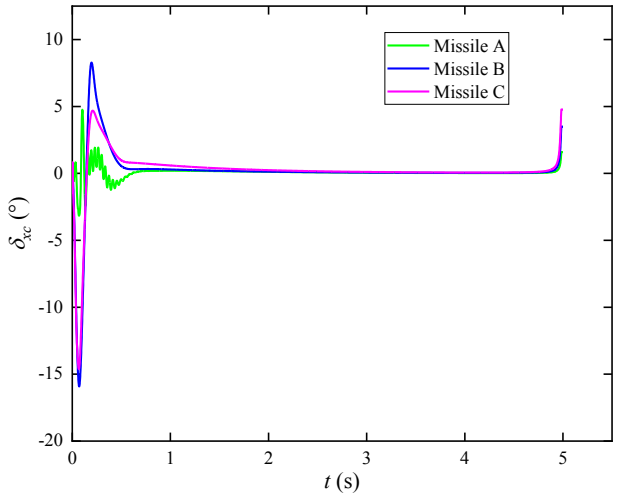

(a)

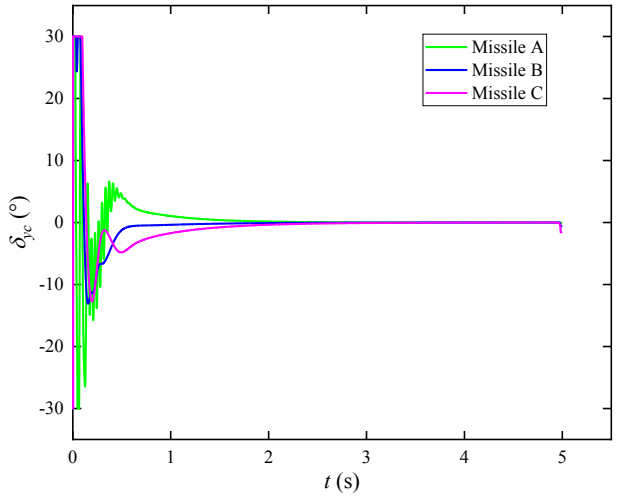

(b)

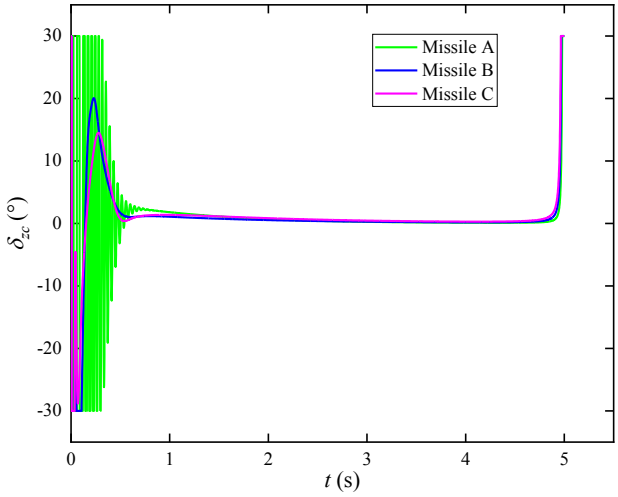

(c)

Fig. 9. Curves of control inputs δ_{xc}, δ_{yc}, and δ_{zc} for three missiles in Case 1.

Figure 9 shows that although the three missiles initially show saturation inputs in both the pitch and yaw channels, the duration is short and there is still a design margin.

Case 2 *Ground-maneuver target*

The effectiveness of the proposed CIGC scheme was verified by simultaneously attacking a ground-maneuvering target using three missiles. The velocity of the ground target is $V_T = 30$ m/s, and the initial velocity-deflection angle is $\psi_{VT0} = 0°$. The target performs a sinusoidal maneuver with a normal acceleration of $a_{tz} = 10 * \sin(\pi t)\ m/s^2$. Suppose that the coefficients of both aerodynamic forces and moments increase by 20% of their respective nominal values.

Table 4 Simulation results for Case 2.

	T_d (s)	Impact time t_f (s)	q_{2d} (°)	q_{2f} (°)	Miss distance (m)
Missile A	5	4.999	115	115.32	0.9107
Missile B	5	4.999	135	135.57	0.9726
Missile C	5	4.999	160	160.56	0.7053

As shown in Table 4 and Figs. 10–12, all three missiles attacked the ground-maneuvered target accurately. The miss distance was < 1 m. The errors between the actual impact time and the predefined impact time were both 1 ms. The errors between the terminal-impact azimuth and desired impact azimuth were all less than 1°. For the ground-maneuvering target, Fig. 11 shows that the three missile-target distances can quickly converge to the desired range and track the value until they hit the target. This confirmed the effectiveness of the proposed cooperative strategy. Figure 12 shows that the azimuths of the three missiles can quickly converge to the desired azimuths and continue to follow, further confirming the effectiveness of the proposed CIGC scheme.

Similar to Case 1, Figs. 13–14 show that the three attitude angles (α, β, γ_V) and the three angular rates ($\omega_x, \omega_y, \omega_z$) of the three missiles initially oscillate briefly to adjust the missile flight attitudes to satisfy the attack requirements, but then remain stable. As shown in Fig. 15, the rudder angles of the three missiles did not exceed the maximum rudder angle. Figure 16 shows that the rudder angle commands for the pitch and yaw channels of the three missiles initially show saturation inputs but do not last long, indicating that there is still a design margin.

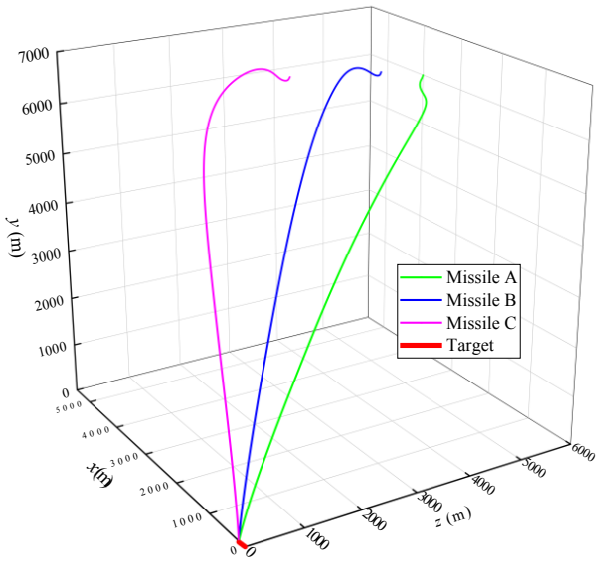

Fig. 10. Trajectories of the target and three missiles in Case 2.

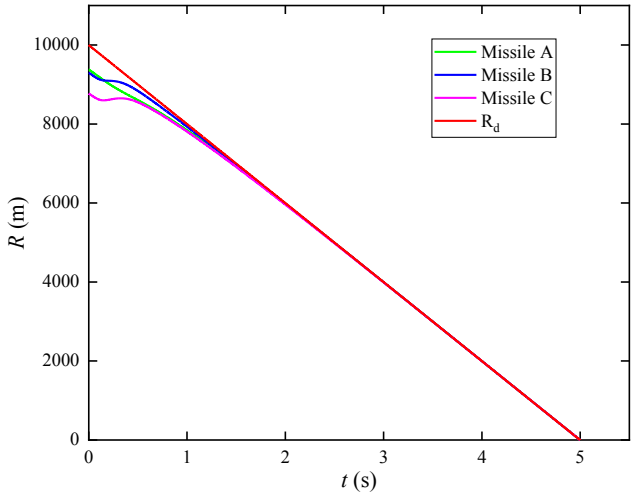

Fig. 11. The three missile-target distance variation curves and nominal ranges follow those in Case 2.

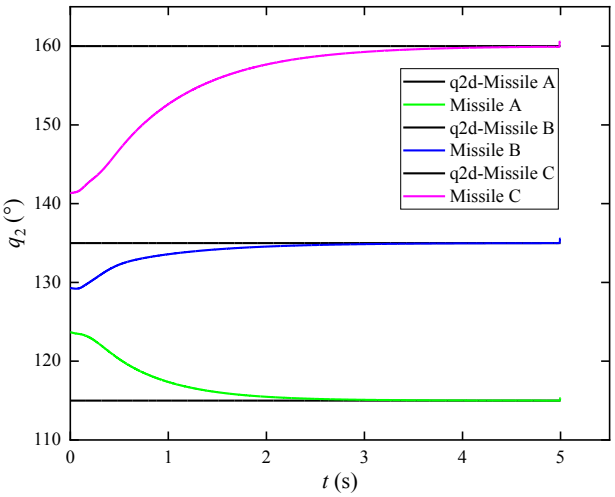

668 **Fig. 12.** Azimuth curves of the three missiles under Case 2.

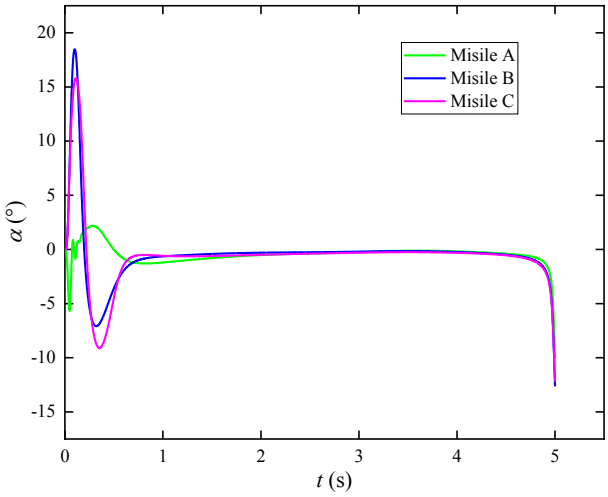

669

670 (a)

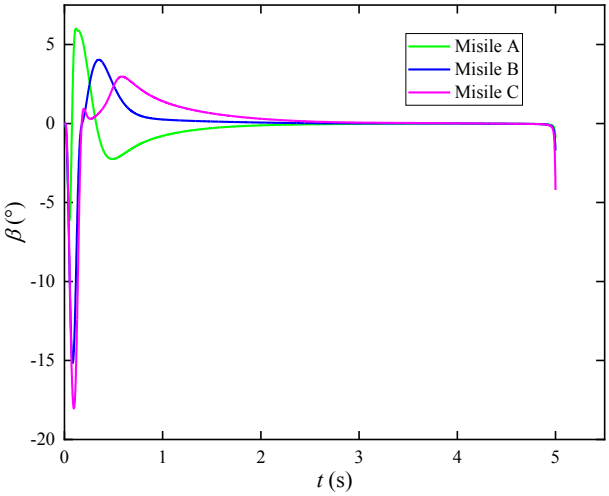

671

672 (b)

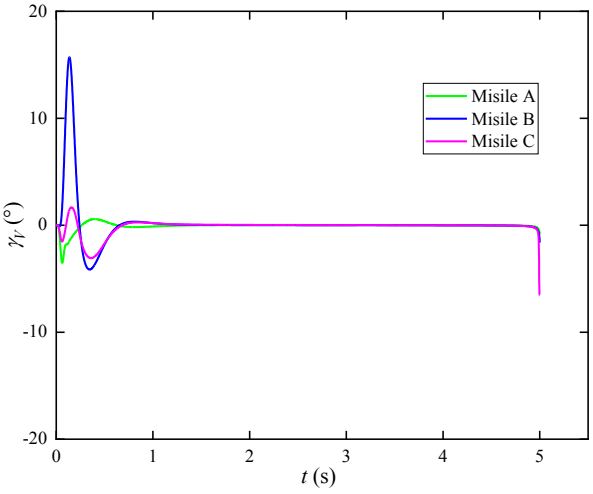

673

674 (c)

675 **Fig. 13.** Curves of α , β , and γ_V for three missiles in Case 2.

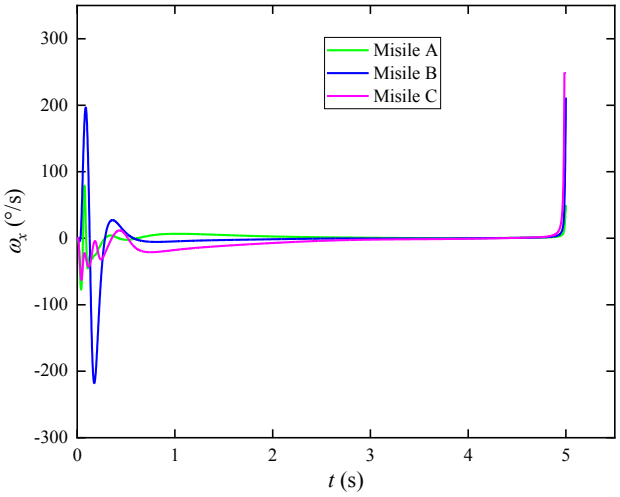

676

677 (a)

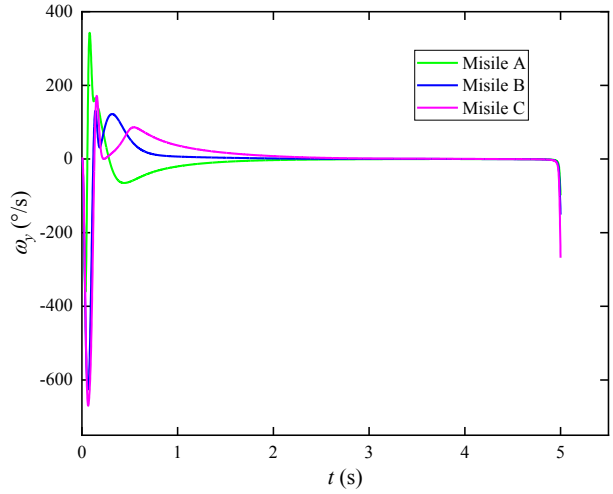

678

679 (b)

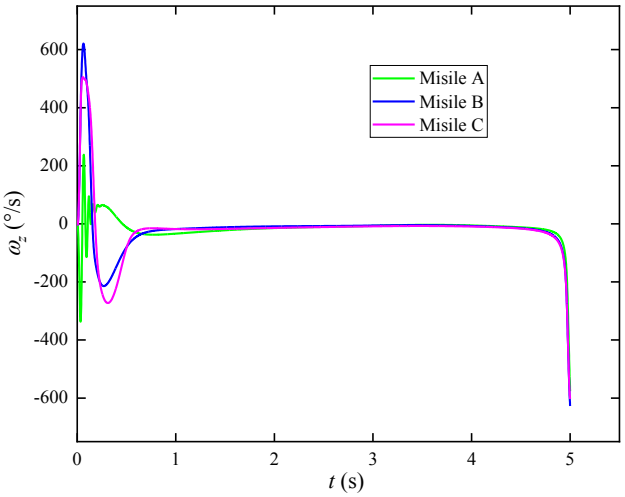

680

681 (c)

682 **Fig. 14.** Curves of angular rates ω_x, ω_y, and ω_z for three missiles in Case 2.

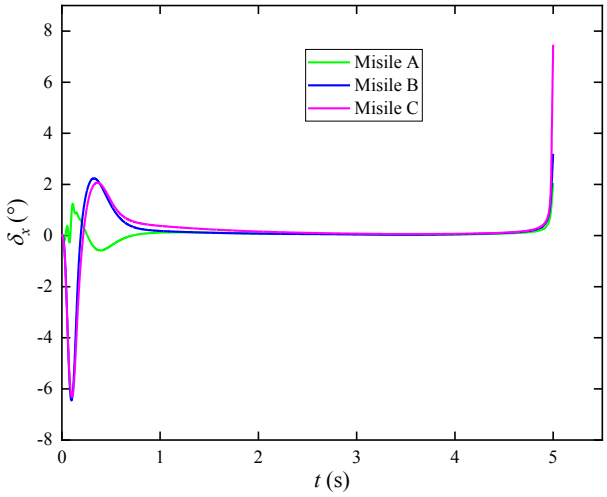

(a)

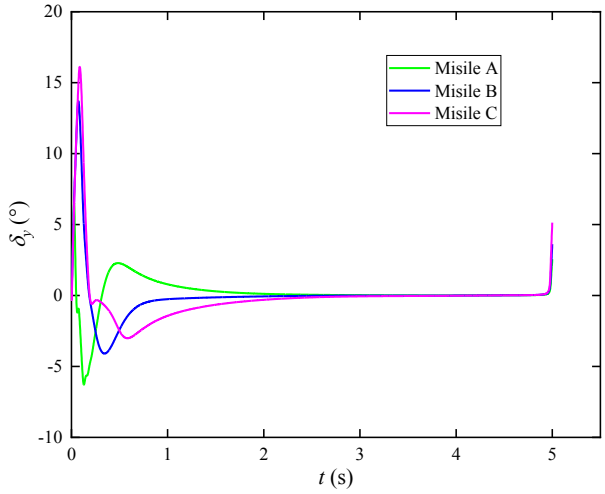

(b)

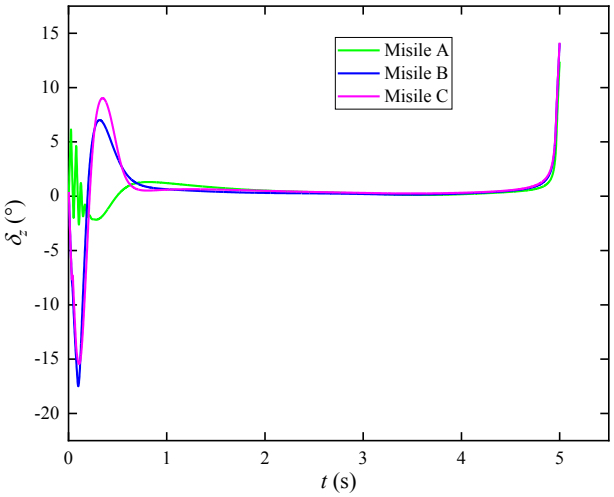

(c)

Fig. 15. Curves of rudder angles δ_x, δ_y, and δ_z for three missiles in Case 2.

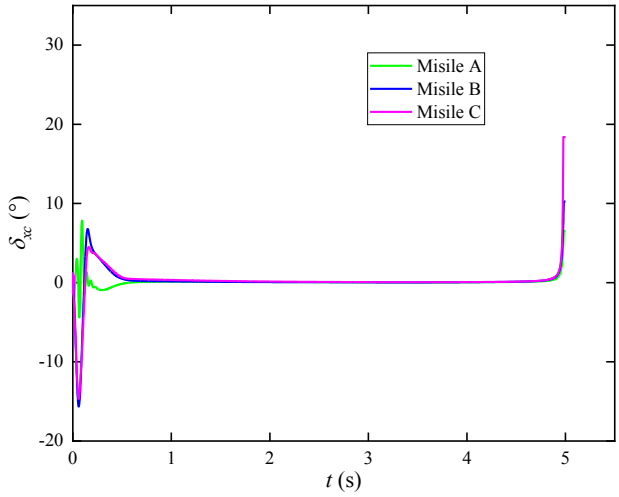

690

691 (a)

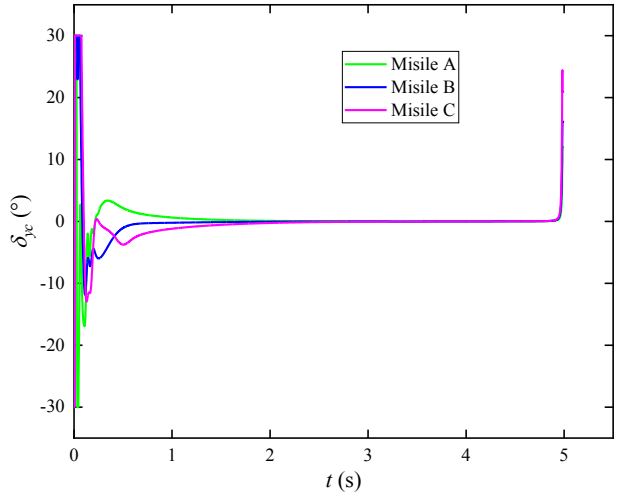

692

693 (b)

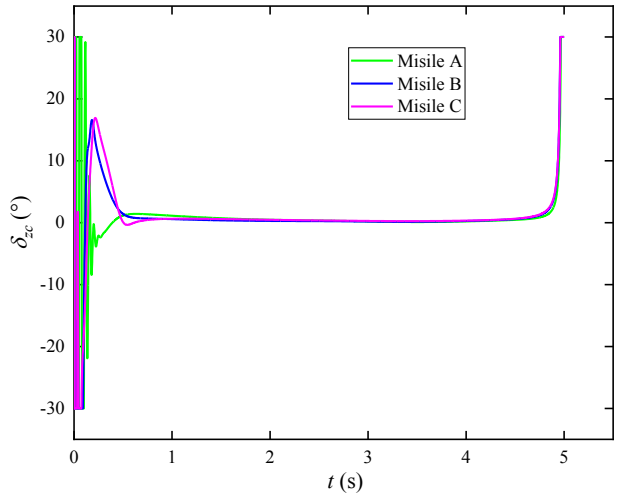

694

695 (c)

696 **Fig. 16.** Curves of control inputs δ_{xc}, δ_{yc}, and δ_{zc} for three missiles in Case 2.

697 **Case 3** *Monte Carlo simulations*

To further demonstrate the robustness of the proposed CIGC scheme, a Monte Carlo simulation with 1,000 samples was conducted. The aerodynamic force and moment coefficients of the missiles were assumed to deviate randomly by ±20% with respect to the nominal values in each sample. The target makes a sinusoidal maneuver, and the acceleration of the target is taken from $5\sin(\pi t) \sim 15\sin(\pi t)$ m/s^2 randomly in each sample. The velocity of the target is $V_T = 30$ m/s and the initial velocity heading angle $\psi_{VT0} = 0°$. The initial position of the missile is located at a random point in a spherical range of 500 m radius with $(4500, 6000, 5500)$ m as the center of the sphere. The desired impact time is $T_d = 5$ s, and the cooperative coefficient is $\gamma = 1.0$.

The simulation results for 1,000 samples are shown in Figs. 17–19. Figure 17 depicts the relative missile position distribution at the moment of interception with the target position at the center of the sphere. It can be seen that all intercept points are almost distributed in a longitudinal plane. Figure 18 shows a box plot of the miss distance, from which it can be seen that the miss distance of all samples is less than 1 m. The average miss distance was 0.941 m, and approximately 50% of them fell within the interval of 0.895–0.973 m. Figure 19 shows a box plot of the terminal-impact azimuth. It can be observed that the errors between the terminal-impact azimuths and the predefined azimuth of all samples are within 1°, with an average error of 0.34°, and approximately 50% falling within the interval of 0.21–0.41°. In summary, the Monte Carlo simulation results further demonstrated the robustness of the proposed CIGC scheme for attacking ground-maneuvering targets.

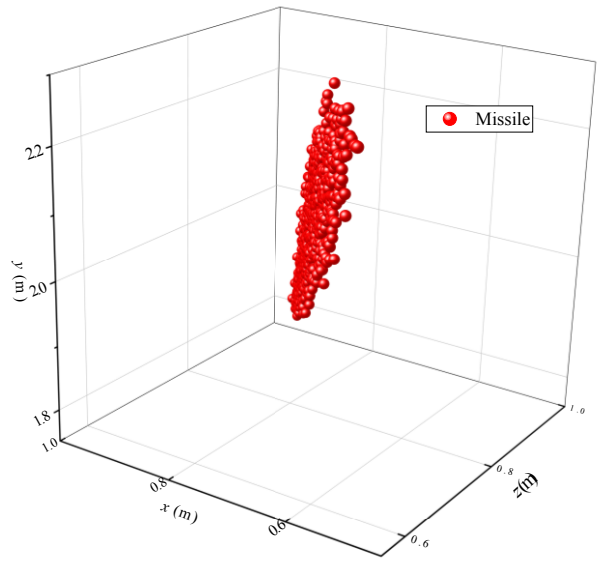

719

720 **Fig. 17.** Interception point distribution of Monte Carlo simulation for Case 3.

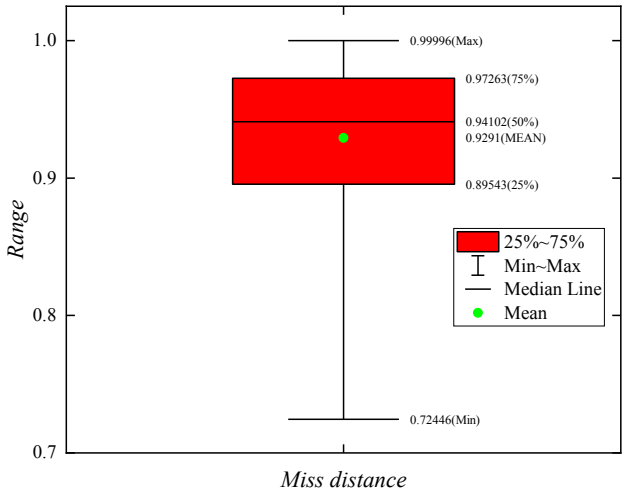

721

722 **Fig. 18.** Missing distance of the Monte Carlo simulation for Case 3.

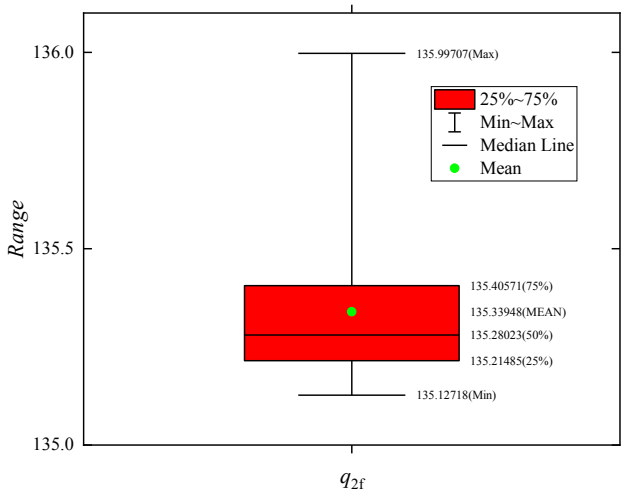

723

724 **Fig. 19.** Terminal-impact azimuths of Monte Carlo simulations for Case 3.

6. Conclusion

A novel three-dimensional (3D) CIGC scheme with fixed-impact azimuth and time constraints was proposed for hypersonic STT missiles attacking ground-maneuver targets. The CIGC scheme proposed in this study only sets the same impact time at the beginning of the terminal guidance. Subsequently, all missiles could simultaneously attack the target without using a communication topology between the missiles. This is helpful for preventing electronic interference from enemy targets, thus improving the penetration probability. Moreover, this enables each missile to attack the target by following its predefined azimuth, thereby further enhancing the destruction effect. In this study, a 3D reduced-order ESO was used to estimate the system-lumped disturbances, avoiding the chattering caused by the introduction of switching terms in the traditional sliding mode control. The proposed CIGC scheme also considers the saturation constraints and delay dynamics of the rudder, thereby improving its execution. The derivatives of the virtual control commands are obtained using DSC, which solves the "differential explosion" phenomenon caused by BC. Monte Carlo simulations further verify the effectiveness and robustness of the proposed CIGC scheme.

Conflict of interest statement

The authors declare no conflict of interest.

745 Appendix A.

Nomenclature			
m	Mass of the missile, kg	V_{Mx}, V_{My}, V_{Mz}	Velocity vectors of the missile in the inertial coordinate system, m/s
g	Gravity acceleration, m/s^2	$a_{Mx4}, a_{My4}, a_{Mz4}$	Acceleration vectors of the missile in the LOS coordinate system, m/s^2
θ_M, ψ_{VM}	Flight path angle and heading angle of the missile, rad	$a_{tx4}, a_{ty4}, a_{tz4}$	Acceleration vectors of the target in the LOS coordinate system, m/s^2
θ_T, ψ_{VT}	Flight path angle and heading angle of the target, rad	α, β, γ_V	Angle-of-attack, sideslip angle and velocity-deflection angle, rad
q_1, q_2	Elevation and azimuth angles of the line-of-sight, rad	ϑ, ψ, γ	Pitch angle, yaw angle and roll angle, rad
R	Missile-target relative distance, m	$\delta_x, \delta_y, \delta_z$	Aileron, rudder and elevator deflections, rad
V_M, V_T	Velocity of the missile and target, m/s	$\delta_{xc}, \delta_{yc}, \delta_{zc}$	Control inputs of aileron, rudder and elevator channel, rad
Q	Dynamic pressure, Pa	J_x, J_y, J_z	Rolling, yawing and pitching moments of inertia, kg/s^2
ρ	Air density, kg/m^3	$c_y^\alpha, c_y^\beta, c_y^{\delta_z}$	Lift force coefficient with respect to α, β and δ_z
S	Reference area, m^2	$c_z^\alpha, c_z^\beta, c_z^{\delta_y}$	Side force coefficient with respect to α, β and δ_y
L	Reference length, m	M_x, M_y, M_z	Roll, yaw, and pitch moments, N • m
Y, Z	Lift and side forces, N	$m_x^\alpha, m_x^\beta, m_x^{\delta_x}$	Rolling moment coefficient with respect to α, β and δ_x
$\mathbf{R}$	Relative distance vector between the missile and target	$m_y^\beta, m_y^{\delta_y}$	Yawing moment coefficient with respect to β and δ_y
$\mathbf{V_R}$	Relative velocity vector between the missile and target	$m_z^\alpha, m_z^{\delta_z}$	Pitching moment coefficient with respect to α and δ_z
$\mathbf{a_R}$	Relative acceleration vector between the missile and target	$\omega_x, \omega_y, \omega_z$	Body-axis roll, yaw and pitch rates, rad/s
$\mathbf{\Omega}$	Angular velocity vector of the LOS coordinate system with respect to the inertial coordinate system	x_M, y_M, z_M	Position of the missile in inertial frame, m
		x_T, y_T, z_T	Position of the target in inertial frame, m

$V_{Mx4}, V_{My4}, V_{Mz4}$	Velocity vectors of the missile in the LOS coordinate system, m/s	τ_x, τ_y, τ_z	Time constant of the aileron, rudder and elevator channel

746

747

References

[1] Y. DING, X. YUE, G. CHEN, J. SI, Review of control and guidance technology on hypersonic vehicle, CHINESE J AERONAUT, 35 (2022) 1-18.

[2] J. In-Soo, L. Jin-Ik, T. Min-Jea, Impact-time-control guidance law for anti-ship missiles, IEEE T CONTR SYST T, 14 (2006) 260-266.

[3] W. Dong, C. Wang, J. Wang, M. Xin, Varying-Gain Proportional Navigation Guidance for Precise Impact Time Control, Journal of Guidance, Control, and Dynamics, 46 (2022) 535-552.

[4] G.K. H., L. H., Composite Guidance for Impact Time Control Under Physical Constraints, IEEE T AERO ELEC SYS, 58 (2022) 1096-1108.

[5] J. YU, X. DONG, Q. LI, Z. REN, J. LV, Cooperative guidance strategy for multiple hypersonic gliding vehicles system, CHINESE J AERONAUT, 33 (2020) 990-1005.

[6] Y. Zhang, X. Wang, H. Wu, Impact time control guidance law with field of view constraint, AEROSP SCI TECHNOL, 39 (2014) 361-369.

[7] X. Chen, J. Wang, Optimal control based guidance law to control both impact time and impact angle, AEROSP SCI TECHNOL, 84 (2019) 454-463.

[8] X. Chen, J. Wang, Two-stage guidance law with impact time and angle constraints, NONLINEAR DYNAM, 95 (2019) 2575-2590.

[9] S. Ma, X. Wang, Z. Wang, Field-of-View Constrained Impact Time Control Guidance via Time-Varying Sliding Mode Control, Aerospace, 8 (2021).

[10] S. HE, C. LEE, H. SHIN, A. TSOURDOS, Optimal three-dimensional impact time guidance with seeker’s field-of-view constraint, CHINESE J AERONAUT, 34 (2021) 240-251.

[11] S. Ma, Z. Wang, X. Wang, Q. Chen, Three-Dimensional Impact Time Control Guidance Considering Field-of-View Constraint and Velocity Variation, Aerospace, 9 (2022).

[12] J. Zhu, D. Su, Y. Xie, H. Sun, Impact time and angle control guidance independent of time-to-go prediction, AEROSP SCI TECHNOL, 86 (2019) 818-825.

[13] Z. Hou, Y. Yang, L. Liu, Y. Wang, Terminal sliding mode control based impact time and angle constrained guidance, AEROSP SCI TECHNOL, 93 (2019) 105142.

[14] Q. Hu, T. Han, M. Xin, Sliding-Mode Impact Time Guidance Law Design for Various Target

776 Motions, Journal of Guidance, Control, and Dynamics, 42 (2018) 136-148.
777 [15] Z. J., Y. J., Guidance Law Design for Impact Time Attack Against Moving Targets, IEEE T AERO
778 ELEC SYS, 54 (2018) 2580-2589.
779 [16] H. Yu, K. Dai, H. Li, Y. Zou, X. Ma, S. Ma, H. Zhang, Three-dimensional adaptive fixed-time
780 cooperative guidance law with impact time and angle constraints, AEROSP SCI TECHNOL, 123 (2022)
781 107450.
782 [17] J. Song, S. Song, S. Xu, Three-dimensional cooperative guidance law for multiple missiles with
783 finite-time convergence, AEROSP SCI TECHNOL, 67 (2017) 193-205.
784 [18] J. ZHAO, S. YANG, Integrated cooperative guidance framework and cooperative guidance law for
785 multi-missile, CHINESE J AERONAUT, 31 (2018) 546-555.
786 [19] X. Yang, S. Song, Three-dimensional consensus algorithm for nonsingular distributed cooperative
787 guidance strategy, AEROSP SCI TECHNOL, 118 (2021) 106958.
788 [20] Z. Chen, W. Chen, X. Liu, J. Cheng, Three-dimensional fixed-time robust cooperative guidance
789 law for simultaneous attack with impact angle constraint, AEROSP SCI TECHNOL, 110 (2021) 106523.
790 [21] G. Li, J. Lü, G. Zhu, K. Liu, Distributed observer-based cooperative guidance with appointed
791 impact time and collision avoidance, Journal of the Franklin Institute, 358 (2021) 6976-6993.
792 [22] C. Ming, X. Wang, R. Sun, A novel non-singular terminal sliding mode control-based integrated
793 missile guidance and control with impact angle constraint, AEROSP SCI TECHNOL, 94 (2019) 105368.
794 [23] Z. Li, Q. Dong, X. Zhang, Y. Gao, Impact angle-constrained integrated guidance and control for
795 supersonic skid-to-turn missiles using backstepping with global fast terminal sliding mode control,
796 AEROSP SCI TECHNOL, 122 (2022) 107386.
797 [24] S. Jiang, F. Tian, S. Sun, W. Liang, Integrated guidance and control of guided projectile with
798 multiple constraints based on fuzzy adaptive and dynamic surface, Defence Technology, 6 (2019) 1130-
799 1141.
800 [25] A. Sinha, S.R. Kumar, D. Mukherjee, Impact time constrained integrated guidance and control
801 design, AEROSP SCI TECHNOL, 115 (2021) 106824.
802 [26] A. Patil, S.R. Kumar, Integrated impact time guidance and control against non-maneuvering targets,
803 Proceedings of the Institution of Mechanical Engineers, Part G: Journal of Aerospace Engineering, 236

(2022) 3327-3343.

[27] A. Sinha, S.R. Kumar, D. Mukherjee, Cooperative integrated guidance and control design for simultaneous interception, AEROSP SCI TECHNOL, 120 (2022) 107262.

[28] X. Wang, Y. Zheng, H. Lin, Integrated guidance and control law for cooperative attack of multiple missiles, AEROSP SCI TECHNOL, 42 (2015) 1-11.

[29] X. Wang, Y. Zhang, D. Liu, M. He, Three-dimensional cooperative guidance and control law for multiple reentry missiles with time-varying velocities, AEROSP SCI TECHNOL, 80 (2018) 127-143.

[30] A. Sinha, S.R. Kumar, D. Mukherjee, Nonsingular impact time guidance and control using deviated pursuit, AEROSP SCI TECHNOL, 115 (2021) 106776.

[31] X.H. Wang, C.P. Tan, L.P. Cheng, Impact time and angle constrained integrated guidance and control with application to salvo attack, ASIAN J CONTROL, 22 (2020) 1211-1220.

[32] R. C., L. X., Y. X., M. S., Extended State Observer-Based Sliding Mode Control of an Omnidirectional Mobile Robot With Friction Compensation, IEEE T IND ELECTRON, 66 (2019) 9480-9489.

[33] T. Chao, S. Quan, P. Ma, D. Zhang, Three-dimensional low-order finite-time integrated guidance and control design with side-window constraint, AEROSP SCI TECHNOL, 121 (2022) 107355.